UiT
THE ARCTIC
UNIVERSITY
OF NORWAY

Faculty of Science and Technology

Department of Physics and Technology

Kara-Siberian sea ice anomaly and its impact on the atmosphere

—

Nozhan Balafkan

FYS-3900 Master's thesis in physics 60 SP, May 2018

Contents

Abstract

The behavior of the autumn and winter weather pattern over Europe and Eurasia was investigated during two periods of high and low ice concentration in September over the Kara-Siberian sea. The ERA-Interim data set (1979-2014) and Monte-Carlo methods were used to capture the anomalous behavior of atmospheric parameters and the statistical significance of the impacted areas. It was found that sea surface temperature shows a statistically significant positive anomaly at the east Siberian sea during September of the low ice years (LIYs) possibly due to intrusion of warm water from the Bering strait due to anomalous behavior fo the atmospheric circulation during September LIYs. Later, during October LIYs, the open water in the east Siberian sea is exposed to cold air above and anomalous energy flux from the ocean to the atmosphere takes place. Additionally, water vapor shows a statistically significant positive anomaly at 1000 hPa level over the east Siberian sea while the 850 hPa shows a minimal anomaly over the same region. Cloud cover was tested over the same region during October LIYs, however, no statistically significant behavior was detected. Furthermore, the geopotential height at 850, 500, and 10 hPa (stratospheric polar vortex) were investigated for the sign of anomalous behavior. All the levels show a negative anomaly over the east Siberian sea, however, the behavior of 850 hPa is not statistically significant. The 500 hPa shows an anomalous behavior at 90 percent significance level and the 10 hPa geopotential height shows a statistically significant negative anomaly over the entire Kara-Siberian sea at both 90 and 95 percent significance levels. Additionally, no statistically significant anomaly was detected in the behavior of the dry static and latent energy convergence/divergence over the Kara-Siberian sea during October LIYs. In terms of precipitation and surface air temperature, northern Europe and central Eurasia appear to be more influenced during the high ice years (HIYs) than LIYs. Precipitation shows a statistically significant positive anomaly over Eurasia during January HIYs and a significant positive anomaly over Europe during February HIYs while there is no significant anomaly during LIYs. Finally, the surface air temperature shows statistically significant anomaly over both Europe and Eurasia during winter HIYs and LIYs, however, the well know "Warm Arctic, Cold Siberia" (WACS) is well detected during December and January of LIYs.

1 Introduction

The Arctic ocean with an approximate area of $\sim$ 14 million Km^2 is thought to play a significant role in regulating the weather pattern of the northern hemisphere and Earth. However, despite its vastness, little is known about its influence over the nearby continents and countries (e.g. Europe, Russia) during different seasons.

It has been shown that in the past few decades the Arctic temperature has been increasing faster than the global average a phenomenon known as "Arctic Amplification". Arctic amplification has resulted in an unprecedented rate of sea ice loss in the Arctic ocean. The coincidence of rapid sea ice loss in the Arctic ocean and the unusually cold and persistent weather patterns observed in northeastern United States, Europe, and Eurasia, specially, in winter season have raised the question whether these extreme phenomena are linked to the rapid sea ice loss in the Arctic ocean. Numerous studies have attempted to answer this question and there appears to be a general consensus within the scientific community that there exists a linkage between Arctic sea ice loss and the extreme weather patterns at mid-latitudes [Kretschmer et al., 2018, Cohen, 2016, Francis and Vavrus, 2015, 2012, Overland et al., 2011]. Regarding the sea ice loss in the Arctic ocean, a great number of studies have paid a special attention to the Barents-Kara section of the Arctic ocean and have shown sea ice loss in this region can alter mid-latitude weather patterns to some extent [Overland, 2016, Mori et al., 2014, Overland et al., 2015]. However, there are disagreements amongst studies regarding the temporal, spatial, and magnitude of these impacts [Sorokina et al., 2016, King et al., 2016]. A significant part of this uncertainty comes from the fact that weather systems (similar to many other natural systems) experience natural internal variabilities. (And sea ice loss in the Arctic ocean is not an exception.) However, the temporal and spatial scale of these variabilities is not fully understood [Chen and Zhao, 2017, Cavalieri and Parkinson, 2012].

Generally, it is thought that the Arctic sea-ice loss can impact the weather patterns at mid-latitude through one of the following feedbacks: immediate and delayed. For a given location such as central Siberia the response time to an immediate scenario could be as fast as a few days to a few weeks while for the same place for the delayed scenario the response time could be inter-seasonal.

In the immediate process, the observed atmospheric circulation anomalies are created as a result of response to the cryospheric changes and the resulting anomalies lead to advection of cold or warm air over different locations [Inoue et al., 2012, Hori et al., 2011].

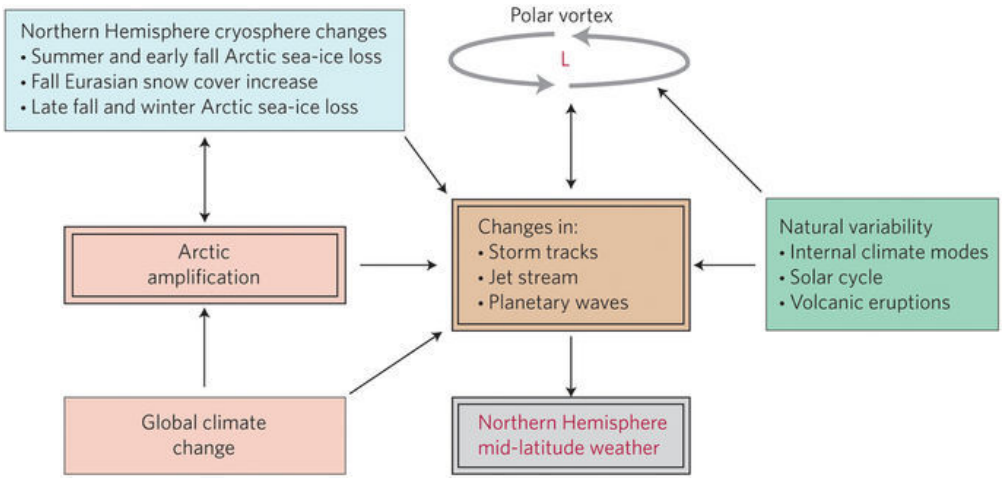

Figure 1: A schematic overview of the contribution of the Arctic sea ice loss to the extreme mid-latitude weather patterns. On the left are the phenomena through which the governing components of the mid-latitude weather patterns (i.e. storm tracks, jet streams, and planetary waves) are altered. On the right are the natural processes that can change the governing components of the mid-latitude weather pattern. The left-hand side factors can either directly or through their contribution to Arctic amplification alter the regulatory components of the mid-latitude weather pattern. Tropospheric polar vortex is the upper most component of this model which through a feedback mechanism can alter the tropospheric and surface atmospheric parameters. [Figure adopted from **?**]

In the delayed response scenario, processes such as Arctic amplification, global climate warming, and changes in northern hemisphere cryosphere alter the storm tracks, jet streams, and planetary waves in northern hemisphere which in turn weaken the stratospheric polar vortex. Eventually, the weakened polar vortex will alter the troposphere and the surface below (Fig. 1).

In this study an attempt will be made to answer the question whether there is a linkage between the Arctic sea ice loss in the Kara-Siberian sea section (60-180° E and 70-82° N) of the Arctic ocean and the mid-latitude weather pattern. The choice of Kara-Siberian sea was made due to the lesser-studied contribution of this region to the weather pattern of the mid-latitude. The structure of the work will be as follows: section 2 describes the theoretical background methods used in this work. In section 3 a summary of the data used in this work will be presented. In section 4 results of this study will be presented along with a detailed discussion of the findings. A special attention will be paid to the impact of sea ice loss at Kara-Siberian section on the atmospheric circulation at lower and mid-troposphere. Finally, in section 5 conclusion will be presented.

2 Background Theory

2.1 Energy Budget and Radiation Balance Near the Surface

Generally, energy budget near the surface is defined as the energy received or lost by the surface via radiation and/or turbulent heat fluxes. The following equation is a simplified representation of the energy budget near the surface,

$$E_s = R_{\uparrow} + R_{\downarrow} + H_{\uparrow} + H_{\downarrow} \tag{1}$$

where E_S is the total energy budge of the surface, $R_{\uparrow}$ is the reflected shortwave and emitted longwave radiation from the surface to the atmosphere, $R_{\downarrow}$ is the absorbed radiation by the surface, $H_{\uparrow}$ is the turbulent heat lost by the surface, and $H_{\downarrow}$ is the turbulent heat component gained by the surface.

In Eq.1, the radiation and heat terms can be further divided into their building components. The following equation shows a more detailed version of the Eq. 1

$$E_s = R_{S\uparrow} + R_{S\downarrow} + R_{L\uparrow} + R_{L\downarrow} + H_{S\uparrow} + H_{S\downarrow} + H_{L\uparrow} + H_{L\downarrow} \tag{2}$$

where R_S and R_L indicate the short and longwave radiation while H_S and H_L show the sensible and latent heat components. Also, as in Eq. 1, the $\uparrow$ and $\downarrow$ arrows show the direction of the energy going out and to the surface respectively.

In the context of energy budget near the surface, signs and directions play a crucial role, however, the connection between the two can become quite confusing. In order to avoid any confusion, the ECMWF sign/direction rule is followed where a "+" sign of any components of the Eq. 2 shows gain of energy by the surface and a downward direction while a "−" sign shows the loss of energy by the surface and an upward direction. For instance, heat flux of $H_{L\uparrow} = -100\ \frac{W}{m^2 s}$ is an indication of the latent heat flux leaving the surface toward the atmosphere. And a flux of $R_{L\downarrow} = +100\ \frac{W}{m^2 s}$ indicates absorption of downward long wave radiation by the surface. Figure 2 shows a schematic view of the energy budget near ice surface.

The short wave radiation terms ($R_{S\uparrow} + R_{S\downarrow}$) become quite weak over the Kara-Siberia sea during autumn and winter. So, this term does not have significant contribution during these months. However, it will be included in the total energy budget.

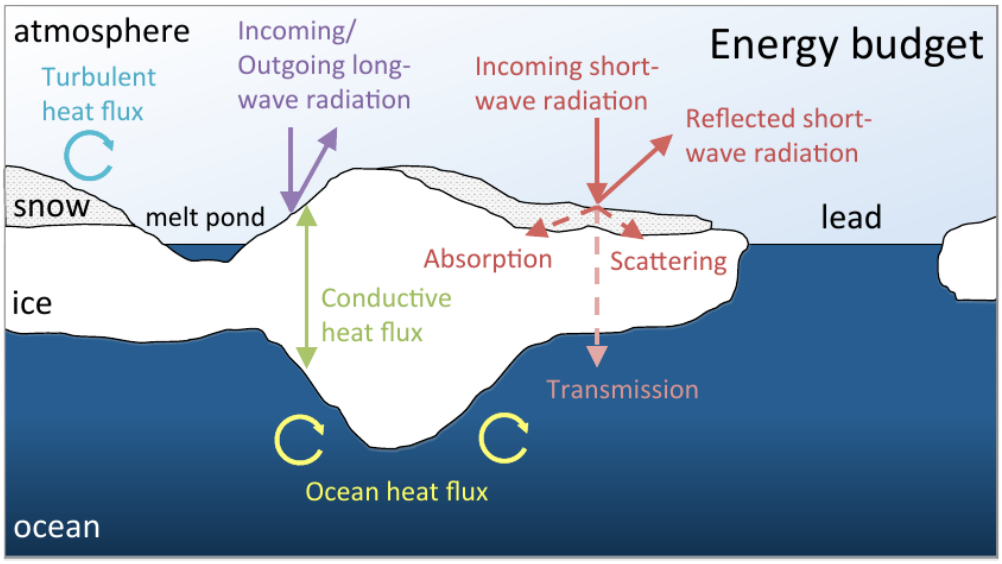

Figure 2: A schematic view of different energy budget component at an ice surface [Credit: Arndt [2016]]

2.2 Energy Transport

Energy transport in earth's climate system is the result of cooperation between oceans and atmosphere. This cooperation reaches its peak value of 5.5 PW (1 PW = 10^{15} W) at 40 N/S Yang et al. [2015]. Generally, the atmospheric heat transport (AHT) is the dominant mechanism in poleward of 30 N/S and oceanic heat transport (OHT) is the dominant mechanism in the tropical region.

2.2.1 Atmospheric Energy Transport

Energy in the atmosphere is transported through air mass motion. It is worth noting how this energy enters the atmosphere in the first place. In its simplest form, the difference between the net heat flux at the top of the atmosphere (TOA) and at the surface is the amount of energy trapped inside the atmosphere (eq. 3).

$$E_{atm} = \int_{\frac{\pi}{2}}^{\phi} \int_{0}^{2\pi} (F_t - F_s) R_e^2 \cos\phi d\lambda \tag{3}$$

Where E_{atm}, F_t, F_s, R_e, λ, and ϕ are total energy in the atmosphere, heat flux at TOA, heat flux at the surface, radius of the Earth, longitude and latitude respectively. AHT mechanism can be further divided into two components: dry static and latent energy components. In

the following, these two components will be discussed in more details.

2.2.2 Dry Static and Latent Energy

Atmospheric heat transport is a simple yet very powerful tool in explaining large scale atmospheric phenomenon around the globe [Graversen et al., 2011]. As stated earlier, energy transport in the atmosphere is the result of air mass motion. There are two key words in this statement: air (mass) and motion. The former is a scalar while the latter indicates velocity where the vector property of velocity can be used to find the direction of the motion. Although air mass is a scalar it still has important properties such as energy. There are two types of heat energy that can be associated with an air mass depending on the water content of the air mass: dry static and latent energy. Dry static energy is the heat content of an air mass with zero water/vapor content while latent energy depends on the water/vapor content of the air mass. Using dry static and latent energy one can define a useful atmospheric parameter called "moist static energy". It can be computed via the following equation

$$h = c_p T + q_v L + gz \tag{4}$$

where c_p is the heat capacity of the dry air mass at constant pressure, T the temperature, q_v the specific vapor value, L the latent heat of vaporization of liquid water, g the acceleration of gravity and z the altitude. Equation 4 is the result of the sum of three energy terms. Regarding this equation, an air parcel at temperature T, humidity q, and height z with respect to a reference point (usually the Earth surface) contains a specific amount of energy. Conservation of the moist static energy through atmosphere under adiabatic and hydrostatic transformation is what makes this parameter very appealing to use [JunIchi and P., 2017].

Earlier it was discussed that energy transport is based on two key components: air mass and motion. Having found the energy content of an air mass, one can combine the energy component and velocity of an air mass to find the exact value of the energy transported across different longitudes and latitudes at different altitudes. Thus, the total vertically integrated meridional and zonal energy transport components in the atmosphere can be approximated respectively as follows

$$J_\lambda = \frac{1}{g}\int_0^1 v(\frac{1}{2}\mathbf{u}\cdot\mathbf{u} + c_pT + gz)\frac{\partial p}{\partial \eta}d\eta \tag{5a}$$

$$J_\phi = \frac{1}{g}\int_0^1 u(\frac{1}{2}\mathbf{u}\cdot\mathbf{u} + c_pT + gz)\frac{\partial p}{\partial \eta}d\eta \tag{5b}$$

where $\mathbf{u} = (u, v)$ is the horizontal wind with v as the meridional (northward) and u as the zonal (eastward) components, η is the vertical hybrid coordinate used in the ERA-Interim reanalysis (see Sec. 3), and the rest of the parameters are similar to the ones in Eq. 4.

The J_λ and J_ϕ components together form the total energy transport vector. On the other hand, it is well know that the divergence of a vector will reveal information on the divergence and convergence property of the vector. Here, a similar approach can be taken to investigate at a gien location whether horizontal energy transport converges or diverges at that point. The following is the energy divergence equation at a given longitude and latitude

$$\nabla\cdot\mathbf{J} = \frac{1}{R_e\cos\phi}\left[\frac{\partial J_\lambda}{\partial\lambda} + \frac{\partial J_\phi\cos\phi}{\partial\phi}\right] \tag{6}$$

where R_e os the Earth's radius, λ longitude, and ϕ is the latitude.

It needs to be noted that for the purpose of this work during the rest of this work a slightly different set of equations were used.

$$\mathbf{J}_{dry} = \frac{1}{g}\int_0^1 \mathbf{v}(\frac{1}{2}\mathbf{v}\cdot\mathbf{v} + c_pT + gz)\frac{\partial p}{\partial \eta}d\eta \tag{7a}$$

$$\mathbf{J}_{latent} = \frac{1}{g}\int_0^1 \mathbf{v}Lq\frac{\partial p}{\partial \eta}d\eta \tag{7b}$$

where g is gravity, $\mathbf{v}(u, v)$ is the horizontal wind with v as the northward and u as the eastward component, c_p is the specific heat capacity of moist air at constant pressure, T is temperature, z is geopotential height, p is pressure, L is the specific heat of condensation/evaporation, q is the specific humidity and η is the vertical hybrid coordinate used in the ERA-Interim reanalysis.

2.3 Atmospheric Circulation

Atmospheric circulation is a large scale mechanism by which energy is distributed across the planet at different latitudes and longitudes. The large-scale circulation is accomplished through three smaller-scale components: Hadley cell, Ferrel (mid-latitude) cell, and polar cell at both norther and southern hemispheres.

2.3.1 Hadley Cell

The Hadley cell is closed circulation loop that extended from equator to 30-40 latitude. Solar insulation energy is at its maximum at the equator. The resulting radiation causes surface heating at large scale which in turn leads to deep air convection to upper atmosphere. The convection process leaves a low pressure region at the surface. The air mass at higher altitudes moves toward the poles (due to pressure difference). As the air mass moves toward poles it cools and converges at 30-40 latitudes. The convergence of the air mass at higher altitudes, also, creates a high pressure region at the surface at this latitudes. Finally, the cooler air moves along the surface toward the equator to balance the low pressure region that was created due to deep convection. These processes form the closed circulation of the Hadley cell.

As stated in the previous paragraph, the existence of low pressure areas in the equator and high pressure areas in the 30-40 latitude results in a pressure gradient force from high to low pressure regions. As the air mass starts to move from high pressure regions to low pressure regions the Coriolis force takes effect and the air mass is deflected to the right of its motion. This results in an easterly (from east to west) wind close to the surface and westerly (from west to east) wind in the upper atmosphere in the Hadley cell.

2.3.2 Ferrel Cell

Ferrel cell, similar to Hadley cell, is a closed atmospheric circulation loop that extends from 30-40 to 60-70 latitudes. Unlike Hadley and polar cells Ferrel cell is not direct result of solar insulation at the surface but rather a response to the ongoing wave activity. Therefore, circulation, in this cell is weaker than that of the Hadley and polar cells. Thus, the driving force, and the resulting atmospheric circulation, is noticeably weaker. The interaction between polar cell and Ferrel cell at 60-70 latitude lifts air to the upper atmosphere leaving behind a low pressure area at the surface at this latitude. The lifted air moves toward the

equator. While it moves toward lower latitudes it cools and it sinks at 30-40 latitude (see Hadley cell). Similar to Hadley cell the pressure difference between the high and low areas within the Ferrel cell creates a pressure gradient force the tends to move the air mass from high to low pressure region. Deflection of the air mass due to the effect of Coriolis force creates a westerly wind on the surface and an easterly wind in the upper atmosphere within the Ferrel cell at mid-latitudes.

2.3.3 Polar cell

Polar cell is extended from 60-70 latitude to 90 in both poles. Air is lifted to the upper atmosphere at 60-70 latitudes and moves toward the poles and it cools and sinks at the poles. At higher altitudes, winds are easterly. However, at the poles the air sinks and creates a region of high pressure at the surface. Then this air mass moves toward the 60-70 low pressure area as a direct result of pressure gradient force. Following this motion and due to Coriolis force westerly wind form at the surface.

2.3.4 Jet Stream

Jet streams are direct result of conflict between pressure gradient force and Coriolis effect at upper atmosphere where the geostrophic wind condition is valid. As discussed above, the air mass under the influence of pressure gradient force will move from high to low pressure regions. However, due to Coriolis force its motion is deflected until there is a balance between the two forces. This balance causes a deflection of wind toward right (in the northern hemisphere) and left (in the southern hemisphere). There are several jet streams in action at different latitudes and altitudes. Polar jet stream at northern hemisphere circulates at 60-70 (and altitude of 8-12 km), and the sub-tropical jet stream around 30-40 (at altitudes of 14-16 km) at northern hemisphere. Typically, 250 mb and 100 mb pressure level maps represent the spatial and temporal evolution of the polar and sub-tropical jet streams.

2.3.5 Geostraphic Balance

In order to explain the geostraphic balance, the following forces are needed: gravitational, pressure, friction, and the Coriolis force (an apparent force). These forces can horizontally interact with an air parcel (an element of air).

A moving object in a rotating system will experience the well known apparent force called

Coriolis force. An air mass with velocity $\mathbf{V}$ will experience the same force under the following governing equation

$$C = \mathbf{f} \times \mathbf{V} \tag{8}$$

where C is the Coriolis vector, $\mathbf{f}$ is the Coriolis parameter given by $f = 2\omega\sin(\theta)$, and $\mathbf{V}$ is the velocity of an object.

In order for an atmosphere to be in hydrostatic balance, the pressure gradient in vertical direction has to be counter balanced by a change in density multiplied by acceleration due to gravity

$$\frac{\partial p}{\partial z} = -gz \tag{9}$$

Equation 9 is the hydrostatic equation. It should be noted that the negative sign in the equation shows that pressure and height follow opposite behavior (increase in height corresponds to decrease in pressure).

Pressure gradient, also, has horizontal components

$$\mathbf{P} \equiv -\frac{1}{\rho}\nabla p \tag{10}$$

or, in component form,

$$P_x = -\frac{1}{\rho}\frac{\partial p}{\partial x} \tag{11a}$$

$$P_y = -\frac{1}{\rho}\frac{\partial p}{\partial y} \tag{11b}$$

where the direction of this pressure gradient is from high to low pressure.

Additionally, the friction force exerted on an air parcel is given by

$$\mathbf{F} = -\frac{1}{\rho}\frac{\partial \tau}{\partial z} \tag{12}$$

where τ is the vertical component of the shear stress (with units of N m^{-2}).

Using the horizontal force components, the time derivative of the horizontal velocity for an air parcel can be written as follows

$$\frac{d\mathbf{V}}{dt} = -\frac{1}{\rho}\nabla p - f\mathbf{k} \times \mathbf{V} + \mathbf{F}. \tag{13}$$

Typically, the magnitude of the horizontal acceleration experienced by an air parcel in large scale wind systems (e.g. extra-tropical cyclones) is one order of magnitude smaller than that of experienced due to Coriolis force. Also, in the free atmosphere where the friction effect over an air parcel is insignificant, the Eq. 13 can be approximated to the following equation

$$\frac{1}{\rho}\nabla p = -f\mathbf{k} \times \mathbf{V}. \tag{14}$$

Equation 14 is called Geostrophic approximation. It shows that under certain conditions, Coriolis force is the only force that can balance the pressure gradient force. The followings show the components of the Geostrophic equation

$$u_g = -\frac{1}{\rho f_0}\frac{\partial p}{\partial y} \tag{15a}$$

$$v_g = \frac{1}{\rho f_0}\frac{\partial p}{\partial x} \tag{15b}$$

In the northern hemisphere in order for the pressure gradient and Coriolis force to balance one another, the geostrophic wind must blow parallel to the isobars. This way, the high pressure system would be on the right and the low pressure system would be on the left side of the air stream. Consequently, the wind flow around a low pressure system would be cyclonic and anticyclonic around a high pressure system (Fig. 3)

2.3.6 Geopotential Height

Geopotential (Φ) can be defined as the amount of work that has to be done to raise a mass of 1 kg against the Earth's gravity from sea level to a point at a certain height (z). It has the unit of J kg^{-1} or m^2 s^{-2}. In a mathematical form this transport from z to z + dz can be written as

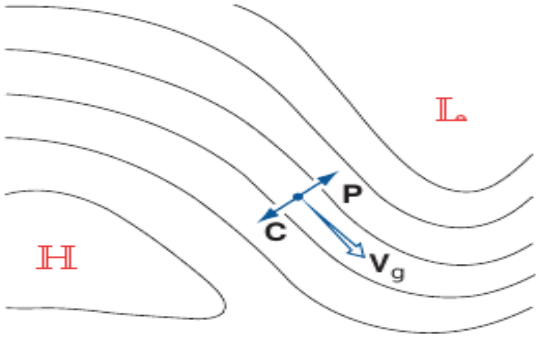

Figure 3: The direction of geostrophic wind around a high and low pressure system. Pressure gradient is from high to low and the Coriolis force acting as a balancing force and the geostrosphic wind is parallel to the isobars. [Credit: Wallace and Hobbs 2006]

$$d\Phi \equiv gdz, \Phi(z) = \int_0^z gdz \tag{16}$$

where the $\Phi(0)$ is the work done at level pressure where it is equal to zero. Thus, geopotential height only depends on the height between the initial point and the final point. This height can be found, simply, by dividing the geopotential height by g as follows

$$Z \equiv \frac{\Phi(z)}{g_0} = \frac{1}{g_0}\int_0^z gdz \tag{17}$$

where Z is the geopotential height and g_0 is the globally averaged value of the g taken as 9.81 m s^{-2}.

3 Data

3.1 Data Assimilation

Measuring atmospheric parameters at different locations is not always possible. However, advances in numerical forecast models of weather systems have made it possible to acquire information on weather conditions of the remotest places with an acceptable level of accuracy. These models are, usually, based on "data assimilation" technique. In this technique, a numerical weather model is run with an initial set of observational values. After a fixed time interval, the output values of the model are compared with the a new set of observational values (acquired at the same time). The validity of the model is checked and the input values of the model are updated with the new set of observational data and this process is repeated. This way a through map of atmospheric data over the entire globe can be constructed. Furthermore, old and present day sets of data can be fed into the data assimilation algorithms to construct a global map of atmospheric data that can capture global climate change for an extended period of time. The application of data assimilation technique to old sets of data to monitor the evolution of the atmospheric parameters is called "reanalysis".

3.2 ERA-Interim

ERA-Interim is the latest global atmospheric reanalysis of its kind (after ERA15 and ERA40) developed by the European Centre for Medium-Range Weather Forecasts (ECMWF). This model is based on a climate reanalysis data set that has been generated with a sequential data assimilation scheme, advancing forward in time and receiving new set of data every 12 hours. In each cycle the new observations are combined with the output values of the model to forecast the evolution of the climate model. The observational data form a wide range of atmospheric parameters such as temperature, pressure and wind at different altitudes, and surface parameters such as rainfall, soil moisture content, and sea-surface temperature. The spatial resolution of the data set is approximately 80 km on 60 vertical levels from the surface up to 0.1 hPa [Dee et al., 2011]. The ERA-Interim spans a time interval of 1979 to present and it is continuously updated in real time (i.e. once per month) though for the purpose of this work data reanalysis from 1979 to 2014 was used.

3.2.1 Model grid box and time step

Generally, weather and climate models are based on discretized equations of fluid dynamics (e.g. continuity) coupled with models of other physical phenomenon such as radiation. Due to the discretized nature of these models, their outputs show the value of atmospheric parameters at separate locations. The distance between these discrete point usually shows that resolution of these models. ERA-Interim uses an 80 km models resolution. That means the distance between two discrete points in ERA-Interim is 80 km. Generally, models will not be able to pay attention to any atmospheric phenomena at distances below their defined distance between two discrete points. The discretization can happen at horizontal (i.e. east-west and south-north), vertical, and in time.

Horizontal Discretization

In horizontal, the discrete points run in two different directions; west-east and south-north. The result is a 2D surface called "grid" and the comprising discrete points are called "grid points". If the distance between grid points in a grid is kept constant (i.e. square) it is a regular grid while if it varies, it is called an irregular grid. In case of a regular 2D grid, the created square area by the grid points on the corners is referred to as the "grid box" (see Fig. 4 for an illustration of the constructed grid box in ERA-Interim model).

All of the atmospheric parameters calculated by the numerical models are attributed to the grid boxes where each grid box represents an area of 80 $\times$ 80 km (in ERA-Interim). For instance, a 2m temperature of 10 Kelvin associated with a grid box, represents the surface temperature of the entire area covered with that grid box which in turn the box is enclosed by a pair of longitudes and latitudes.

Vertical Discretization

A similar approach to spatial discretization can be taken, however, this time a one dimensional height discretized levels will be implemented. Vertical dimension in the ERA-Interim model is defined by an eta (η) coordinate (Fig. 5). In the eta coordinate, pressure is a function of surface pressure and two time-independent coefficients a and b where these coefficients are a function of height. The following shows the pressure as a function of surface pressure, a, and b.

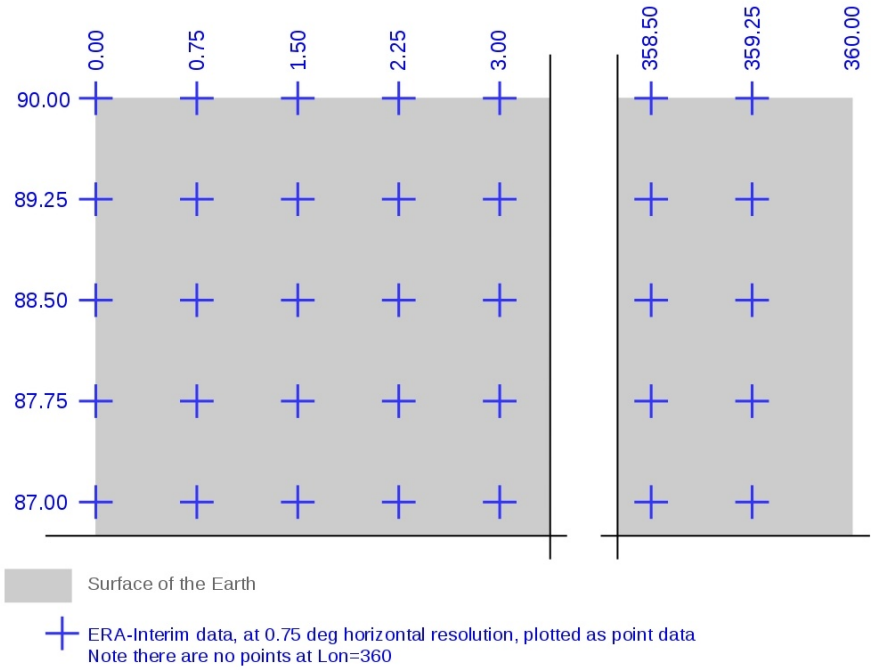

Figure 4: A schematic view of the grid points in 2D horizontal grid. [Credit: ECMWF]

$$p_k(\lambda, \phi, t) = a_k + b_k P_s(\lambda, \phi, t) \tag{18}$$

Where k is the vertical index, λ longitude, ϕ latitude, t time, and P_s is the surface pressure. The above equation plays a significant role in computing the vertical integrals, derivatives, and interpolation schemes. Also, 18 is used in computing geopotential height which is a finite difference form of derived fields.

Time Discretization

Generally, weather and climate models return their outputs at fixed time intervals (e.g. 00:00 or 12:00). These models use smaller discrete time intervals called "time step" to advance through time and reach the time at which the outputs must be returned. This process is repeated until the end of the simulation has reached. Usually, the length of time steps varies from a few minutes to half an hour depending on the model and the purpose of the model.

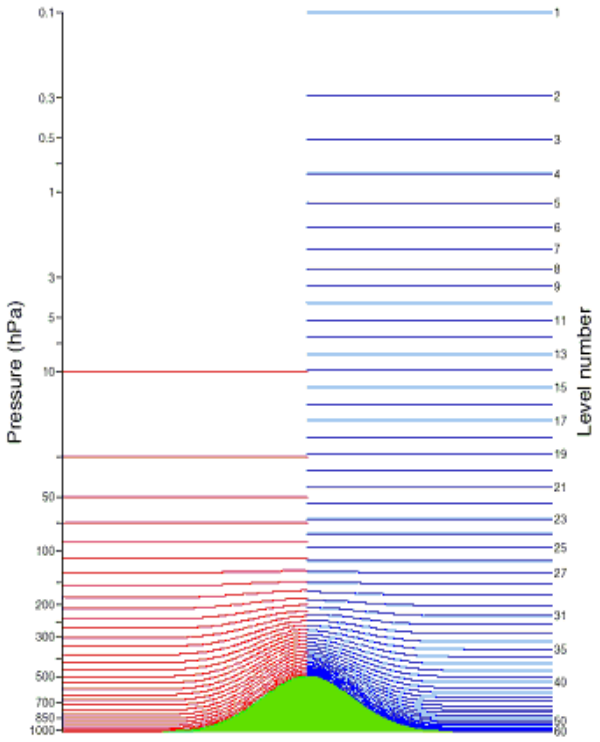

Figure 5: A schematic comparison of the eta and pressure levels in ERA-15 (red lines), ERA-40 and ERA-Interim (blue lines). The number of eta levels has increased from 31 in ERA-15 to 60 in ERA-40 and ERA-Interim. [Credit: ECMWF]

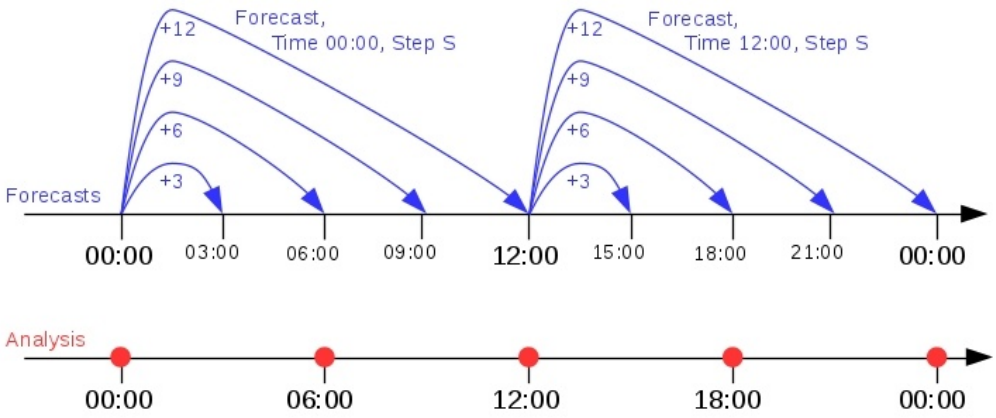

Figure 6: A schematic view of the time steps in the analyses and forecast datasets. [Credit: ECMWF]

3.2.2 Dataset in ERA-Interim

Generally, ERA-Interim datasets fall into one of the following categories: analyses, forecasts. The analyses dataset is comprised of data outputs of the ERA-Interim model on a daily basis and four times per day at 00:00, 06:00, 12:00 and 18:00. On the other hand, for a given time interval the forecast datasets can be reached on different time steps (for example for the interval 00:00 and 12:00, time steps can be set to 3, 6, 9, and 12-hour steps, and more, into the future). Figure 6 shows a schematic view of the similarities and differences between the two data sets.

3.2.3 Instantaneous and Accumulated Parameters

All the atmospheric parameters in the analyses dataset and many of the parameters in forecast datasets (e.g. Temperature and pressure) belong to the instantaneous class of data. It should be noted that here instantaneous doe not mean at very short time steps (e.g. seconds) but it refers to the 30-minute time steps of the ERA-Interim model. In addition to instantaneous data type, a second class of data called accumulated exist. Only forecast values fall into this class data. Depending on the value of the forecast time step, the values of the atmospheric parameters are accumulated at each time step and is output at the end of each time step. Precipitation and radiation fluxes are two examples of such data class.

3.2.4 ERA-Interim: monthly means

The followings are four different types of monthly means in ERA-Interim:

- Synoptic Monthly Means (mnth), where the average is taken at four synoptic hours of 00, 06, 12, and 18 UTC for the analyses data or at 3, 6, 9, 12 time steps of the 00 and 12 UTC of the forecast data.
- Monthly Means of Daily Means (moda): this average is only taken at synoptic hours of 00, 06, 12, and 18 UTC for the analyses data and the instantaneous parameters of the forecast data.
- Monthly Means of Daily Forecast Accumulations (mdfa): this average is similar to "moda" except the average is taken over the accumulated parameters such as radiation and precipitation.

For the purpose of this work "moda" and "mdfa" were used. See table 1 for a more detailed view of the different types of parameters used in this work.

3.3 Data Types

Table 1 shows a list of the atmospheric parameters that were used in this study. This table does not provide the entire details of each individual parameter but only the ones that are relevant to this study. As a good practice, the reader is advised to use the "parameter ID" column in each row to see a more detailed overview of each parameter in the "Parameter Database" section of the ECMWF website [1].

The followings are short notes on some of the parameters in the table.

- For all parameters the monthly means were used except the dry static and latent energies.

- In order to find the total precipitation convective precipitation, Convective snowfall, large-scale precipitation, and large-scale snowfall were added together.

- In order to find the cloud cover the vertical integral of total column liquid cloud water and vertical integral of total column frozen cloud water (referred to as the liquid cloud water and frozen cloud water in the table) were added together.

- To find the total energy budget at the surface surface net solar radiation, surface net thermal radiation, surface sensible heat flux, and surface latent heat flux were added together.

- The ECMWF website states that "by model convention downward fluxes are positive".

[1] https://bit.ly/2Ij9rJ4

- Radiation and heat flux parameters (all together 4 parameters) were divided by 86400 s to convert their values from J m^{-2} to W m^{-2}.

- Dry static and latent energy were not taken from the ERA-Interim directly but they were computed using Eq. 5 (see Sec. 2).

Name	Short Name	Units	Parameter ID
Sea-ice cover	ci	(0 - 1)	31
Specific humidity	q	kg kg^{-1}	133
Sea surface temperature	sst	K	34
Convective precipitation	cp	m	143
Convective snowfall	csf	m of water equivalent	239
Large-scale precipitation	lsp	m	142
Large-scale snowfall	lsf	m of water equivalent	240
liquid cloud water	—	kg m^{-2}	—
frozen cloud water	—	kg m^{-2}	—
Geopotential	z	m^2 s^{-2}	129
Surface pressure	sp	Pa	134
2 metre temperature	2t	K	167
Surface net solar radiation	ssr	J m^{-2}	176
Surface net thermal radiation	str	J m^{-2}	177
Surface sensible heat flux	sshf	J m^{-2}	146
Surface latent heat flux	slhf	J m^{-2}	147
Dry static energy	—	—	—
Latent energy	—	—	—

Table 1: Table of the atmospheric parameters used in this study. Notice that the

3.4 Monte Carlo Simulation

The main part of the analysis in this study is to capture the anomalous behavior of the atmospheric parameters and, further, to find the statistical significance of the anomalous behaviors. Since this study is based on a climatological sample (1979-2014) and sub samples of the climatological sample, Monte-Carlo method seems to be an appropriate choice in finding the statistical significance of the anomalous behaviors.

The essence of the Monte-Carlo methods is based on repeated random sampling in which a series of randomly selected samples (from the parent sample) are compared against their parent sample to check whether a certain condition is met. (In this study the checking step happens at every single grid point.) In this study the focus is on anomalous behavior of atmospheric parameters. In this study, in order to find anomaly, the climatological average

was subtracted from the average of the subsamples. The result is the deviation from zero value at each grid point. Therefore, for example, the behavior of an atmospheric parameter is said to be significantly different from zero at a confidence level of 95 percent if less than 5 percent of the grid points at randomly selected subsamples have a value larger than that of the original sample. The repeated random sampling step can be done as many time as needed. In this study the number of iteration is set to 5000. This means that 5000 subsamples of randomly selected and ordered years from the parent sample (1979-2014) were created.

4 Result

The aim of this work is to investigate a possible linkage between summer SIC extent at Kara and east Siberian Seas (KSS) and the weather pattern over the European continent and Eurasia. (Here sea ice concentration is defined as any grid cell with more than 15% ice content.) To probe this possible linkage, different atmospheric parameters and their correlations will be investigated in the following sections. Also, in order to avoid unnecessary repetition and confusion, the following abbreviations will be used throughout the rest of this work (see table 2).

Abbreviation	Complete form
KSS	Kara and east Siberian Seas
HIYs	A period of high SIC over KSS during September
LIYs	A period of low SIC over KSS during September
CC	Cloud coverage
EE	Europe and Eurasia
LWD	Downward Long Wave
SAT	Surface Air Temperature
SIC	Sea Ice Concentration
SST	Sea Surface Temperature

Table 2: Table of abbreviations that will be used in this section.

The findings of this study will be presented and discussed in the following order. First, sea ice loss and the possible mechanisms behind it will be discussed (e.g. wind forcing and sea surface temperature). Next, the anomalous behavior of several atmospheric parameters with a focus on SAT, precipitation, and latent energy divergence/convergence will be investigated. Finally, in the last section, an attempt will be made to provide an explanation for the observed behavior of the investigated atmospheric parameters and their possible linkage.

4.1 Sea Ice Concentration over Kara-Siberian Sea

In order to explore a possible connection between summer SIC over the KSS and EE weather pattern, it was decided to compare the behavior of the atmospheric parameters during years with unusually high and low area of SIC over the KSS in their summers (i.e. HIYs and LIYs). It was found that the SIC over KSS reaches its lowest during August (see Fig. 8), however, September SIC was selected since the difference between SIC in HIYs and LIYs in September is higher than that of the August. Also, the selected set of HIYs and LIYs are identical in September and August, except for one year.

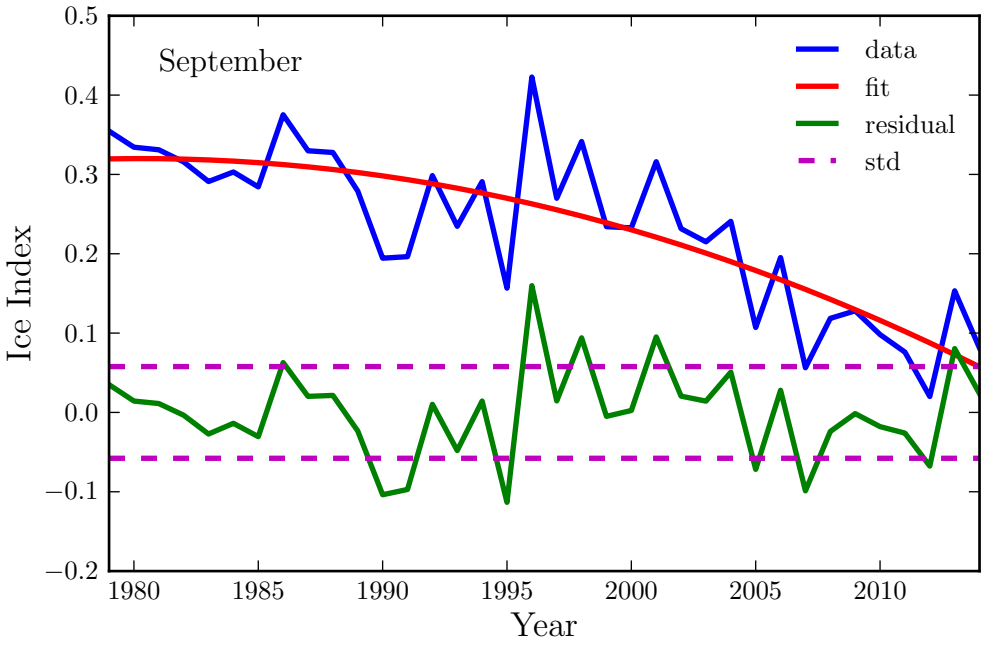

Figure 7: In order to find years with anomalously high and low SIC over KSS a curve was fit (red line) to the SIC index time series (blue line) and the fit was subtracted from the time series. The residual line (in green) shows the diversion from the average at each year. One standard deviation (dotted line in purple) was used to select years with anomalously high and low SIC.

Next, in order to find years with lowest and highest SIC in September, the climatological time series of the SIC index over KSS was made. It is important to notice that the SIC index does not give us any information regarding the shape or thickness of the sea ice but only the fraction of ice in each grid point and it extends from 0 to 1 where 0 shows no sea ice cover and 1 shows full sea ice cover in each grid cell.

The time series covers an interval of 36 years (1979-2014). It is clear that the SIC follows a decreasing trend towards the year 2014. The next step is to find the best fit to the data sample. For a time series with a straight line behavior (i.e. slope of zero) the process of finding the best fit can be achieved, simply, by finding the average value of the time series. However, as a result of the strong decreasing trend the behavior of this time series is far from a straight line and this trend introduces a bias to the data since most of the years toward the end of the time series will fall below the average value. This bias results in an underestimation of the number of high years and overestimation of the number of low years. In order to neutralize the effect of this trend, the data need to be detrended. To do so, a second degree polynomial was fit and subtracted from the original data. What is left is the detrended data from which the high and low years were selected. To select HIYs and LIYs, 1 σ standard deviation was used as a threshold. The choice of 1 σ was the result of a

compromise between making a statistically meaningful sample of years while only retrieving true LIYS and HIYS. Table 3 shows years at which the SIC index is at its highest or lowest state during the August of that year.

Ice Coverage	Year
High	1986,1996,1998,2001,2013
Low	1990,1991,1995,2005,2007,2012

Table 3: Both high and low years during which the 1σ condition of the SIC index was met.

Using 1σ condition, the low ice years of 2005, 2007 and 2012 were captured. Also, a closer look reveals that the choice of threshold has resulted in a fair distribution of the years with half of the LIYs before 2000 and the other half after 2000. A similar behavior can be seen in HIYs.

In order to have a better picture of the SIC index over KSS during the selected years, a map of the summer SIC (during September) over the entire Arctic region was made (Fig. 8).

It is clear from the map that the KSS is almost deprived of SIC during its low state. On the contrary, in its high state, most of the Siberian sea is covered with ice. However, Kara sea shows a lack of ice coverage even during the high years. Looking at the climatological average, the Kara sea is almost ice free during September. Therefor, it is possible that any linkage between SIC over the KSS and EE weather pattern is more connected to Siberian sea than Kara sea since there is a noticeable change in SIC over Siberian sea in HIYs and LIYs (see Fig. 8-d).

4.2 Energy Budget at the Surface

A number of studies have investigated the impact of radiation and turbulent heat fluxes at the surface over the Arctic region [Cao et al., 2017, Kapsch et al., 2016, Meiji et al., 2008]. Energy imbalance at the surface in the Arctic ocean has been suggested as a contributing mechanism behind the Arctic warming by affecting the surface and atmosphere through gain and loss of anomalous values of energy. For instance, Cao et al. [2017] have used a long-term (1984-2014) spatially complete satellite data to investigate how downward longwave (LWD) radiation, water vapor, cloudiness are connected and what their contribution to Arctic warming is. They find that there is a strong correlation between increased water vapor and cloudiness and LWD in winter and spring time. In a different study, Yiyi et al. [2016] focused on 16-year trends of Arctic springtime cloud and radiation properties on September sea ice retreat and found a positive correlation between LWD and springtime cloud. On the other hand, Joseph

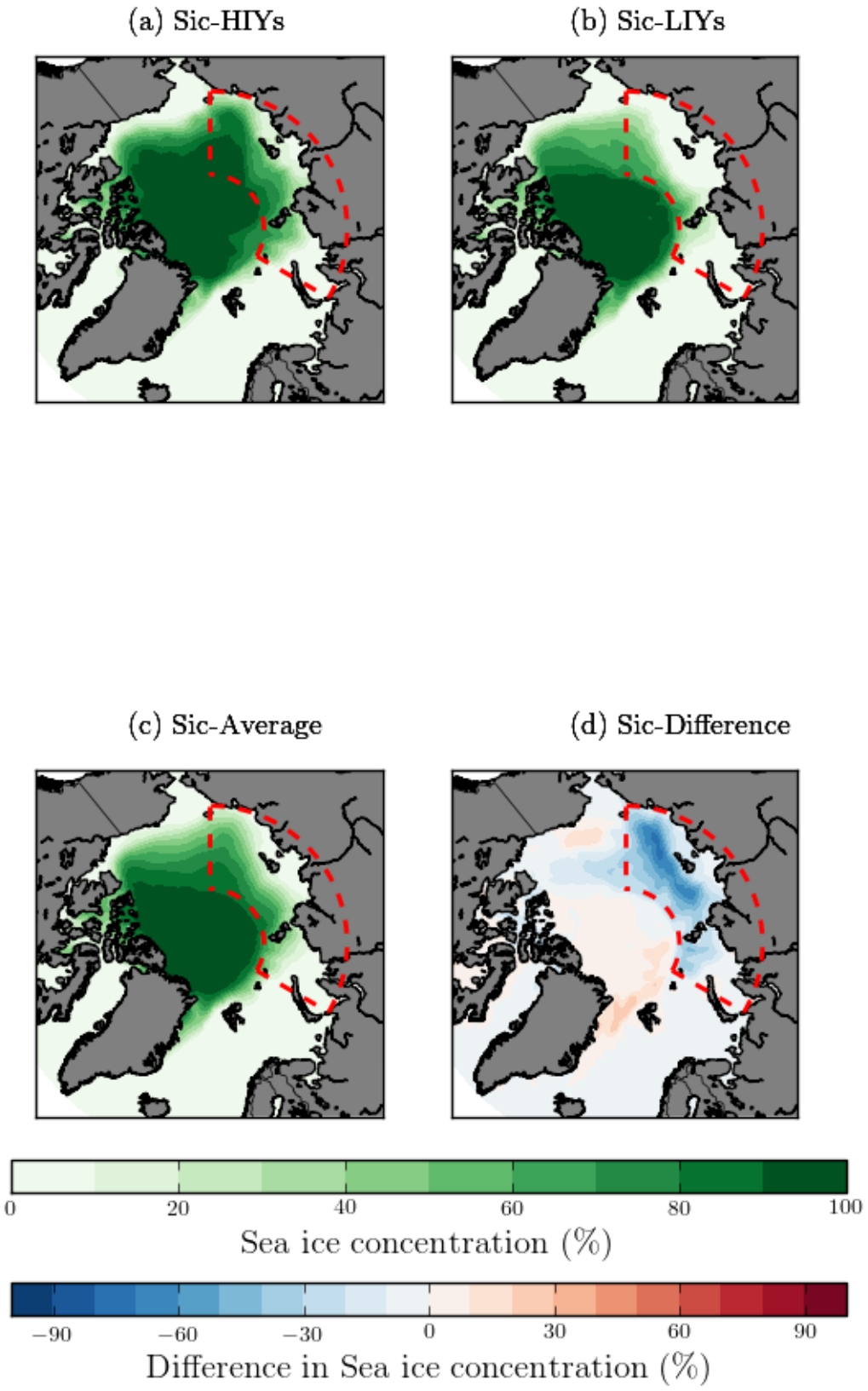

Figure 8: Summer SIC over the KSS at four different states; high (a), low (b), average (c), and low - high SIC state (d). The red green shading shows the SIC while the red and blue shadings show the difference between SIC in low and high SIC states. Also, the area enclosed by red dashed lines show the KSS.

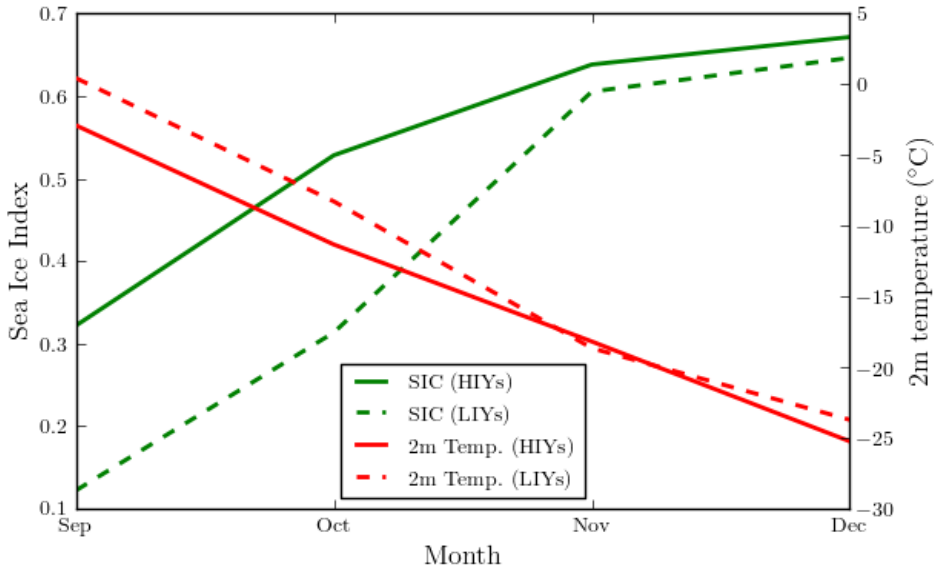

Figure 9: The behavior of SIC and 2m temperature over KSS during HIYs and LIYs. It is apparent that there is a significant difference between SIC during September and October. However, from October to November this difference decreases rapidly due to higher temperatures of the KSS at LIYs. Red dashed (line) and green dashed (line) show the 2m temperature and SIC during LIYs (HIYs) respectively.

and Michael [2016] found that despite anomalous advection of warm and moist air to Arctic, summer time outgoing longwave radiation (OLR) of 1-4 Wm^{-2} act as a cooling mechanism against Arctic warming.

It is well known that ice cover over ocean acts as an insulator and prevents water from losing or gaining energy. A possible positive energy imbalance (increase of energy more than the average value) for an extended period of time will eventually result in ice thinning or loss processes. Therefor, the insulating criteria of water will weaken and the ocean water below will, finally, start exchanging heat with the atmosphere above through different energy loss and gain mechanisms (e.g. latent, sensible, longwave radiation).

In order to explore the energy budget behavior of the surface and the impact of radiation on energy budget, SIC-2m temperature and energy budget components were plotted (Fig. 9 and 10). Figure 9 shows the behavior of SIC index and area weighted 2m temperature over KSS. A significant difference in SIC index is apparent in September and October which is the direct result of the selection procedure (see section 1.1 for further details). However, from October to November this difference decreases remarkably and the sea ice restores noticeably faster in LIYs.

The fact that KSS's SIC increases rapidly in LIYs indicates that water must be losing a

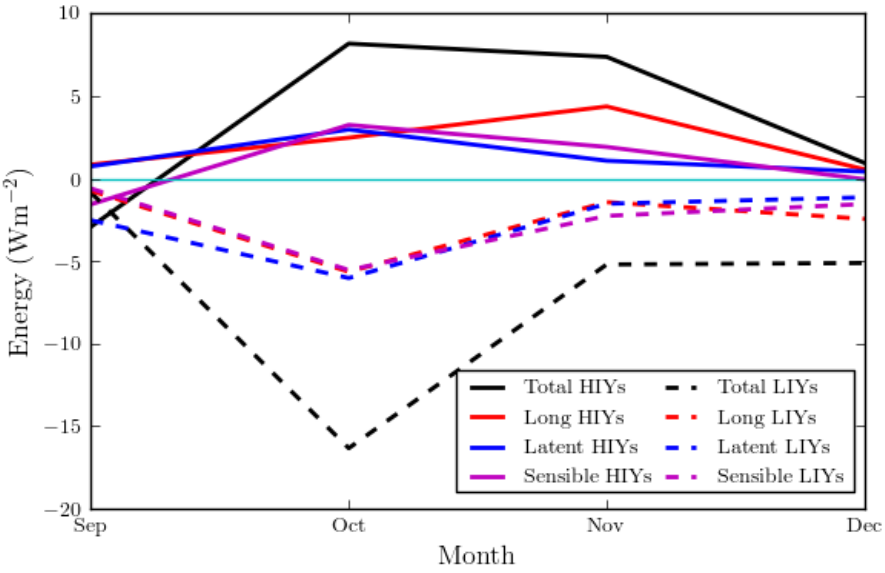

Figure 10: Area weighted average total energy budget anomaly and some of its components over KSS. It is clear that in October and November the surface is losing (gaining) energy during LIYs and HIYs, relative to climatological average, respectively. From September to October the surface loses (gains) energy during LIYs (HIYS) due to its higher (lower) than average temperature. Note that the shortwave radiation is included in the total energy budget but not as a separate component. Solid line and dashed lines show HIYs and LIYs respectively. The thin cyan line shows the zero value. Also, negative and positive values show loss and gain of energy by the surface.

substantial amount of energy compared to its counterpart in HIYs. Also, it needs to be noticed that the temperature over KSS in LIYs is about 3 ℃ warmer than HIYs in October, however, this temperature difference is reduced during transition from October to November until they both have nearly identical temperatures in November.

To investigate energy budget anomaly of the surface over KSS, the total radiation and heat flux balance were plotted for Autumn and Winter months (Fig. 10). There are several noticeable features and an attempt will be made to provide a detailed discussion on these features.

The first feature is the discernible dichotomy in the behavior of the total energy budget of the surface with positive values during HIYs and negative values during LIYs. Such dichotomy reveals that the rate of energy loss from the surface during LIYs on average is higher (more negative) than that of the surface during HIYs. Consequently, the average energy subtraction results in two different patterns of positive and negative values for HIYs and LIYs respectively.

To further explain the observed behavior of the energy components at the surface, it is assumed that the sea surface temperature does not change considerably (due to high heat capacity of the water) during autumn and winter. Since the sea surface temperature (SST) and surface air temperature (SAT) are close, the temperature gradient between them is also small. As a result of the small temperature gradient between them, there is less energy transport between atmosphere and ocean. And that explains the small discrepancy between the total energy budget of the surface in September during LIYs and HIYs. However, as the SAT decreases during autumn the temperature gradient between ocean and atmosphere increases. Consequently, the temperature gradient between them increases and there will be an energy flux from ocean (source with higher temperature) to atmosphere (source with lower energy) the result of which can be seen in Fig. 10. The resulting energy loss of the surface will lead to ice formation and a subsequent increase in sea ice coverage (Fig. 9).

Interestingly, from October to November, there is a decrease between the total energy budget of the surface at HIYs and LIYs while there is an even bigger temperature gradient between atmosphere and ocean. This apparently contradictory behavior can be explained by minimal SIC difference during HIYs and LIYs at November. The existing sea ice acts as an insulator between the ocean water and atmospheric air and reduces the energy flux significantly. Finally, from November to December, a rather distinct behavior is observed during HIYs and LIYs, where in the former, the total energy anomaly decreases and approaches the climatological value while the latter shows no changes in total energy anomaly during transition

from November to December. The resulting constant behavior of the total energy anomaly of the surface during LIYs is due to increasing (decreasing) energy loss (gain) of the surface through infrared radiation and heat turbulent fluxes respectively.

A closer look at the components of the total energy anomaly of the surface at Fig. 10 gives a better insight into the contribution of each component to the energy budget of the surface. It needs to be noted that the net shortwave radiation is included in the total energy budget but not as a separate component in the plot. This is due to the fact that the impact of net shortwave radiation on the surface reduces significantly (specially at higher latitudes) as autumn and winter months approach. A variation in longwave radiation component of the HIYs is distinguishable compared to LIYs where all components follow a rather similar pattern. Such increase in longwave radiation can usually be attributed to higher ice concentration (resulting in less energy to be radiated to the atmosphere) or a sign of presence of cloud coverage over the region. Clouds can block and absorb the incoming shortwave and emit back in longwave radiation.

Although these plots show anomalous behavior of the energy budget, they still cannot provide any information on the statistical significance of the area they are affecting. It is not clear what fraction of these patterns is an exclusive behavior of energy budget during these specific years (i.e. LIYs and HIYs; table 3) and what fraction is the natural behavior (regardless of the choice of years). To overcome this problem, it was decided to indicate the statistical robustness of these anomalies using a Monte-Carlo (MC) approach (see Sec. 3 for more details on MC technique). In order to focus the attention of this study on the linkage between SIC and weather pattern over ENE, only months (either in low or high years) with anomalies that meet the following conditions are shown and discussed,

i) anomalies are statistically significant (i.e. 90 and 95 percentile),

ii) anomalies cover an extended area.

Regarding these two conditions, fig. 11 shows October and November anomaly plots after running MC with 5000 iterations and superimposing 90 and 95 significance levels. It is evident that both sets of years show two distinct pattern over the KSS with positive energy budget anomaly during HIYs and statistically significant negative energy budget anomaly during LIYs. These results are consistence with the total energy budget anomaly plot (see Fig. 10).

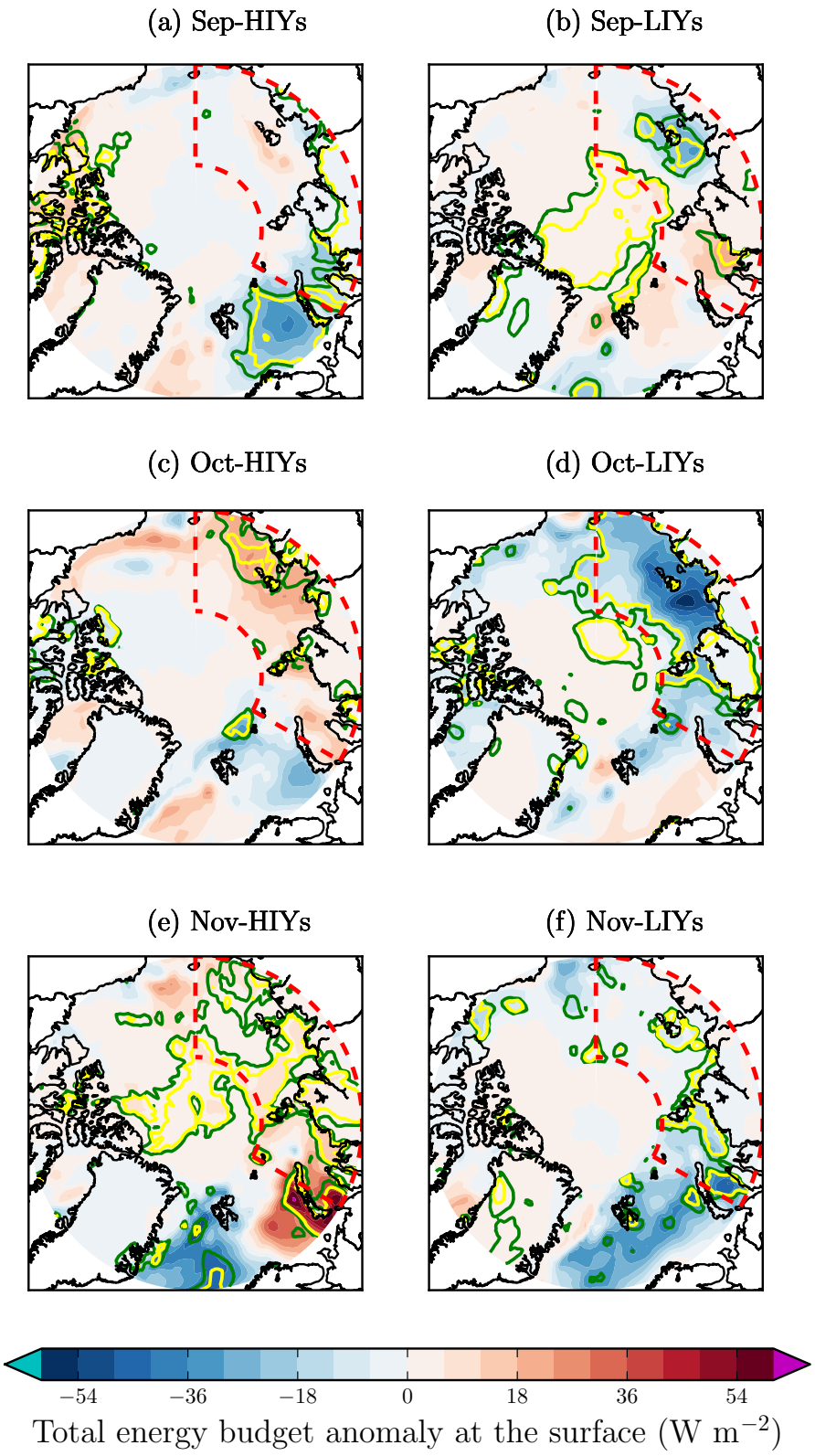

Figure 11: Total energy budget anomaly of the surface northward of 70 latitude. The dashed line shows the area of study (KSS). The green and yellow solid lines show the statistical significance of 90 and 95 percent levels respectively. The distinct negative and positive anomalies of the energy budget is clear in October and to a lesser extent September and November. Surface is losing (gaining) energy at a considerable rate during October and November LIYs (HIYs) respectively. Negative values show an upward direction of the energy (i.e. energy loss by the surface) and positive values show a downward direction of the energy (energy gain by the surface).

4.2.1 Water Vapor

Water vapor can accelerate sea ice loss process significantly [Kim and Kim, 2017, Wenchang and Gudrun, 2016, Woods and Caballero, 2016, Michael et al., 2015]. Zhong et al. [2018] studied two sources of moisture supply for the Arctic warming over the Barents-Kara seas. They found that in a time interval of 37 years (1979-2015) about 57.3% of the water vapor is provided through meridional/poleward transport from lower latitudes and 35.4 % is provided locally. Also, they find that the negative Arctic oscillation-like pattern tend to reduce the advection of water vapor from lower latitudes (external sources). However, the same pattern favors the local evaporation. Wenchang and Gudrun [2016], in a different study, direct their attention to the impact of extreme daily springtime moisture transport events into the Arctic region via Atlantic sector (Atlantic longitudes). They find that the blocking weather pattern over the north Atlantic is the deriving force behind the intrusion of water vapor into the Arctic region. On the other hand, similar to the findings of Zhong et al. [2018], Wenchang and Gudrun [2016] find that the negative north Atlantic oscillation pattern rarely coincides with these extreme water vapor transport events.

In order to have a better understanding of the water vapor content of the atmosphere over the KSS, geospatial plots of water vapor as a function of pressure levels were made (Fig. 12). It is evident that in September, October, and November during both HIYs and LIYs (except October HIYs and LIYs) water vapor shows a statistically significant positive anomaly over KSS. Interestingly, there is a distinct behavior between the LIYs and HIYs water vapor pattern specially discernible at 1000 mb level, that is the anomalous behavior during LIYs happens over the east Siberian sea while during HIYS this pattern is most pronounced over the Kara sea. This behavior can partially be explained based on the distribution of energy budget anomaly and SST at this region. The are of the strong positive water vapor anomaly pattern during September LIYs matches well with that of the SST in the same month (see Fig. 14-b) a sign that warmer SST directly (and mechanisms responsible for warmer SST indirectly) is the driving force behind water vapor anomaly during September LIYs. On the other hand, the October LIYs pattern agrees well with energy budget anomaly at the surface during the same time (October LIYs). A closer look at Fig. 11-d and Fig. 10 shows that during October LIYs the surface looses substantial (anomalous) amounts of energy in the form of latent energy (along with sensible and longwave radiation energies). This loss of energy is a direct result of water evaporation from the surface toward atmosphere. Consequently, the anomalous evaporation leads to an anomalous updraft of water vapor toward atmosphere and, accordingly, the observed patterns (Fig. 12-d). It is very likely that a similar explanation (i.e. energy budget anomaly at the surface) can be able to explain the

observed result in Fig. 12-a, however, the positive anomaly of water vapor in September HIYs is less strong compared to what is seen in September LIYs which can be a result of the less strong energy budget anomaly at the surface during the same time (see Fig. 11-a).

Despite the statistically significant behavior of the water vapor during November HIYs (12-b), the surface energy budget shows anomalously positive values during this month a sign that the surface is gaining energy rather than loosing (Fig. 10 and 11-c). Also, the SST does not show statistically significant positive anomaly during November HIYs (Fig. 14-e). Looking at Fig. 17-g there seems to be a minimal latent energy convergence anomaly during this time. However, this anomaly is insignificant which makes it unlikely to be responsible for the observed anomaly over the KSS (Fig. 12-e and Fig. 17-g). Nonetheless, further analysis is required to explain the observed behavior of the water vapor during November HIYs.

Given the results in Fig. 12, it appears that most of the contribution to the water vapor anomaly over the KSS is the result of local (Fig. 14 and Fig. 11) rather than external forcing (Fig. 17), specially, during September and October.

4.2.2 Cloud Coverage

It is widely accepted that cloud coverage (CC) can positively contribute to sea ice loss process by absorbing and radiating the longwave radiation back to the surface leading to an enhanced longwave radiation feedback [Yiyi et al., 2016, Kapsch et al., 2016, 2013, Semmler et al., 2012]. As a result of this process, the surface cannot lose energy and cool compared to when with sky is clear. In this section CC and its possible contribution to the observed energy budget anomaly over the KSS will be discussed briefly.

Figure 13 shows the CC anomaly for during September and November over KSS (October is not shown since there is no significant anomaly during this month for both HIYs and LIYs). A statistically significant negative anomaly is visible in September during HIYs (Fig. 13-a). On the other hand, a positive anomaly appears in November during HIYs (Fig. 13-c). The negative anomaly over the KSS can be due to an unusually lower updraft of water vapor from ocean to atmosphere. The lower water vapor updraft in turn could be the result of anomalously lower temperature gradient between the ocean and the atmosphere. Or a good ice insulation over an unusually larger area. For a more detailed discussion of the possible sources of the water vapor in the atmosphere over the Artcic ocean see Sec. 4.2.1

It is very likely that the positive CC anomaly in November during HIYs Fig. 13 is connected

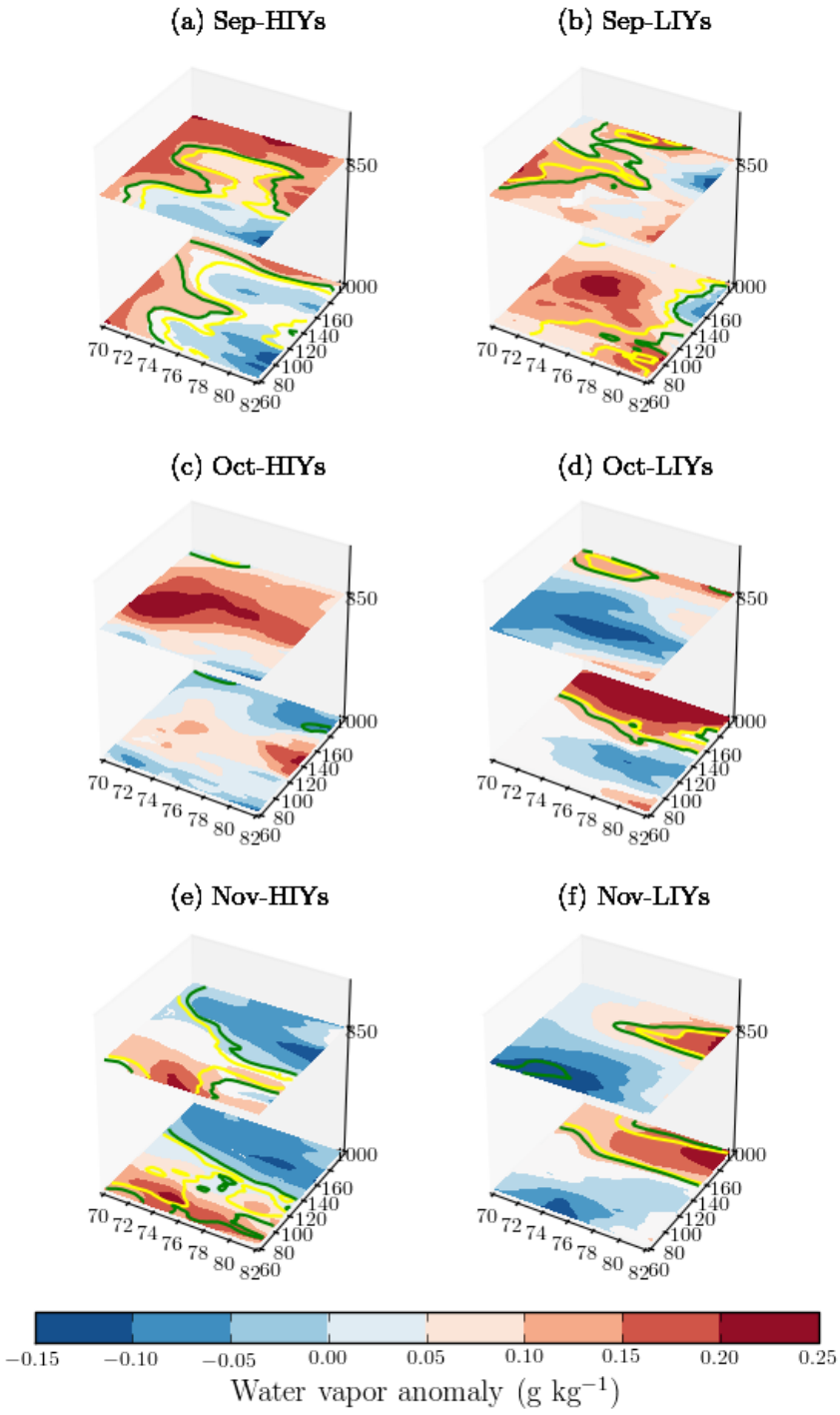

Figure 12: Water vapor anomaly over the KSS at two different pressure levels 1000 and 850 mb (z-axis) during autumn. The longitudes of the Kara ans Siberian seas run from 60 to 100 and 100 to 180 respectively while the latitude of the both runs from 70 to 82 north. Similar to other plots the green and yellow solid lines show the 90 and 95 percent statistical significance. LIYs show a positive anomaly over the Siberian part of the KSS while HIYs mostly show lack of water vapor over the same region. This behavior is particularly clear in 1000 mb pressure level.

to the maximum value of the net longwave radiation component at the surface during the same month in HIYs (see Fig. 10. A probable linkage between the two observed behavior (CC and net longwave) is as follows. Once the cloud forms over the KSS the outgoing longwave radiation is absorbed and radiated back to the surface by the CC. Eventually, this process leads to an anomalously positive net longwave radiation at the surface in November during HIYs.

It is possible that the reduced CC in September HIYs is the result of smaller atmospheric moisture transport from lower latitudes the Arctic region [Semmler et al., 2012].

4.2.3 Sea Surface Temperature

Early sea ice loss in a specific region in the Arctic ocean, usually, leads to a higher sea surface temperature at that location [Michael and Suzanne, 2016]. Although processes through which SST is regulated are not fully understood, there are mechanisms such as wind-driven vertical mixing [Davis et al., 2016], lateral mixing due to instability-driven Eddies and meanders [K. et al., 2015] inflow of warm and fresh water from Bering strait [Watanabe et al., 2017, Woodgate, 2018, A. et al., 2009] that are known to have effect on the behavior of SST in the Arctic ocean. Michael and Suzanne [2016], in their study of the processes that warm the upper ocean during summertime in the Arctic ocean pose the following questions: "What causes the ocean to warm in the Pacific Sector during the summer"? and "What causes sea ice to melt in the Pacific Sector during summer"? In response to their first question, they find that the majority (80 %) of the heat over pacific section of the Arctic comes from ocean surface heat flux and the remaining heat (20 %) comes from the ocean lateral heat flux convergence. Regarding the second question, they find that above-the-surface ice melt is the dominant process during early summer months due to atmospheric heating, while below-the-surface ice melt is the dominant process during late summer due to ocean heat transport. Recently, Zhang et al. [2018], studied the connection between sea ice, SST, and wind speed. They find a negative correlation between SIC and wind, however, the correlation between wind speed and SST is complicated due to the presence of sea ice. Nevertheless, they find that there is a negative correlation between wind speed and SST over open and low ice waters and a positive correlation over high ice waters (see Sec. 4.2.7 for a more detailed discussion of wind and sea ice interaction).

To have a better understanding of SST behavior and anomalies in the KSS, a similar approach to energy budget was followed. First, the climatological average of SST was calculated. Next, the climatological average was subtracted from the average SST of both HIYs and LIYs to

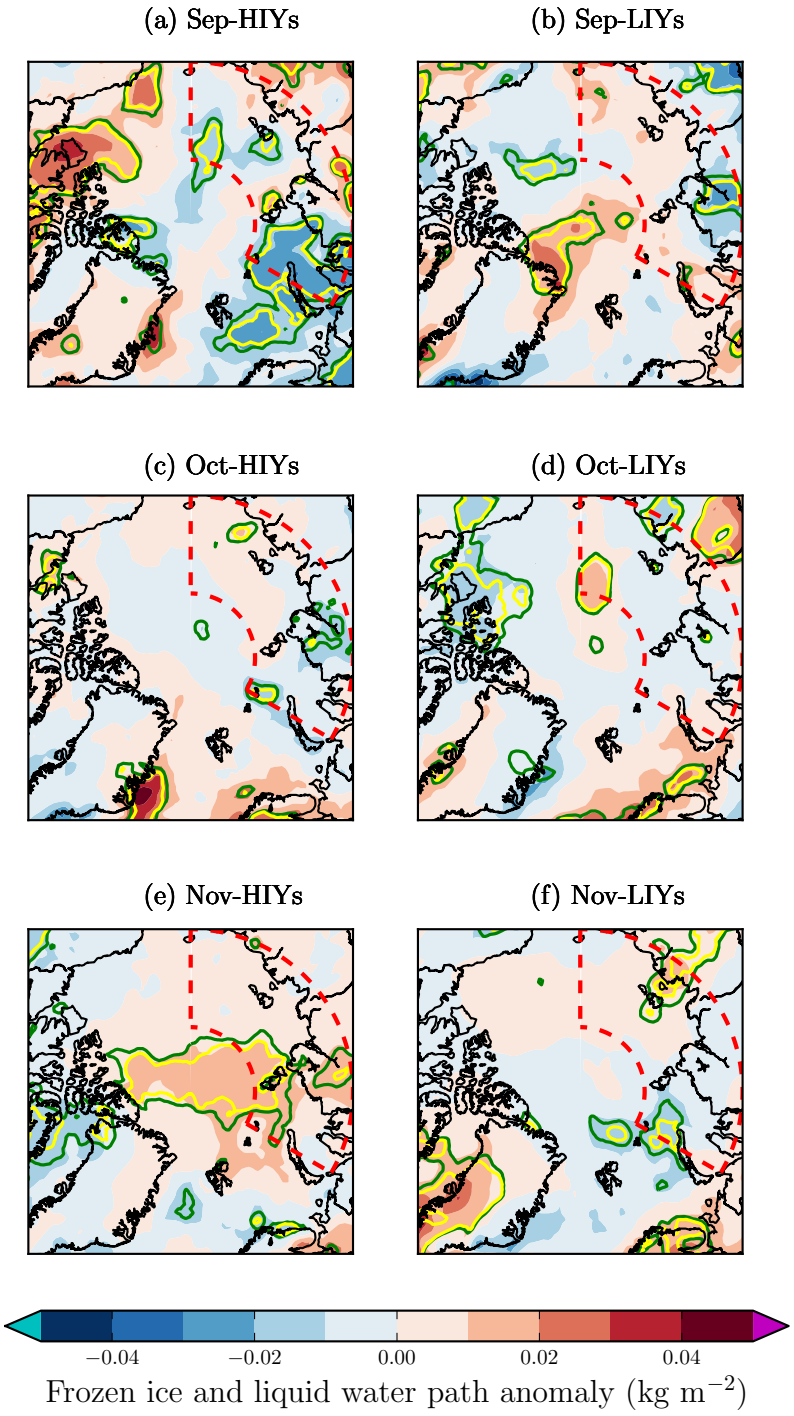

Figure 13: Cloud cover anomaly over KSS during September, October and November. Plot a) shows a statistically significant negative anomaly over KSS during the HIYs possibly due to anomalously low updraft from the ocean to atmosphere or meridional water vapor advection to the Arctic region. On the other hand, November (e) shows a statistically significant positive anomaly over the KSS possibly a response to the surface and lower tropospheric warming of the ocean due to anomalously positive energy budget at the surface in this region. Solid green lines show 90 and solid yellow lines show 95 percent statistical significance. Also, the dashed red lines show the study area (KSS).

find the anomalies. Finally, a MC method was run with 5000 iterations to find the statistical significance of the anomalies. Figure 18 shows the SST anomalies over the KSS during September, October and November.

Unlike LIYs, HIYs do not show statistically significant anomalies over the KSS during autumn except a small negative anomaly in September. The significant anomalies in September and October are probably a result of several mechanisms happening concurrently, however, given the location of high and low pressure systems in September at LIYs (see Fig. 18 for SLP circulation pattern), wind-driven inflow of warm water from Bering strait appears to play a significant role besides other mechanisms (e.g. higher short and longwave radiation and heat turbulent fluxes at the surface, and locally strong winds). Also, the positive anomaly at the Barents and Kara seas during November can possibly be explained by the warm Atlantic water coming through Fram strait and deflected toward this region [Takao and Hiroyasu, 2015, rthun et al., 2012].

4.2.4 Surface Air Temperature

Surface air temperature (SAT) is amongst the most investigated atmospheric parameters and there are a number of studies exploring the impact of AA on SAT in mid-latitudes [Wegmann et al., 2018, Kim and Kim, 2017, Kretschmer et al., 2018]. Despite numerous studies, there is not an agreement amongst them regarding the existence of a linkage between the mid-latitude SAT and AA. Nevertheless, the so-called "Warm Arctic, Cold Siberia" (WACS) is a phenomenon that an increasing number of studies agree on [Wegmann et al., 2018, Lantao et al., 2016, Cohen et al., 2014]. (Also, see Fumiaki et al. [2017] for an opposing argument about WACS phenomenon.) ("Warm Arctic, Cold Continents" is a more general term, however, since the focus of this study is on Eurasia and the European continent the term "Warm Arctic, Cold Siberia" is used here.) This pattern is usually referred to the unusually cold winters over northern and central Siberia while the Arctic ocean is unusually warm. This feature has been found both in observation [Kim et al., 2014] and in model experiments [Pedersen et al., 2016]. However, the origin of this phenomenon still is a matter of debate. Several studies have suggested a delayed response to the sea ice loss in the Barents sea and the resulting stratospheric feedback as the possible explanation behind the WACS [Kretschmer et al., 2018, Cohen et al., 2014]. On the other hand, other studies have proposed a more rapid response to the sea ice loss in Barents sea as the possible driving mechanism behind WACS [Sorokina et al., 2016, Inoue et al., 2012].

As mentioned earlier in this chapter, the aim of this section is to investigate the anomalous

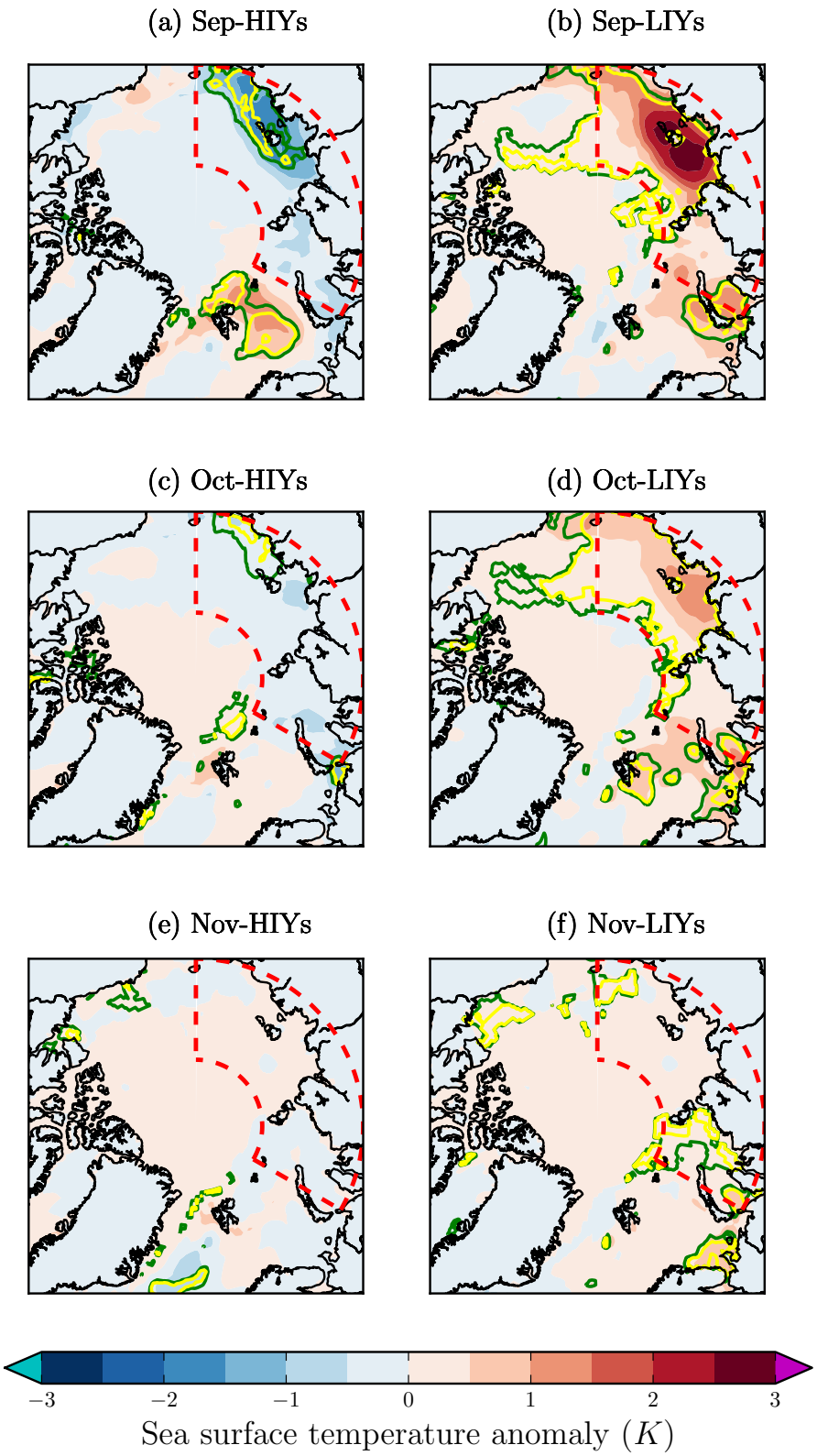

Figure 14: Sea surface temperature anomaly northward of 70 latitude for September, October, and November HIYs and LIYs. Region enclosed by dashed red line shows the area of study (KSS). The green and yellow solid lines show the statistical significance of 90 and 95 percent respectively. There is a clear positive anomaly during autumn of LIYs. It is clear that the anomaly is persistent but smaller as it continues to November (but to a lesser extent).

behavior of the SAT over EE. Since the purpose of this study is to explore the possible impact of sea ice loss (over KS) on the EE weather pattern (here SAT) in winter time, only winter anomaly will be shown here. To fulfill that promise, SAT data are shown and investigate in this section.

Figure 15 shows the surface air temperature (SAT) anomaly northward of 30 latitude. The WACS feature is apparent in January HIYs and it is consistent with the result of the [Wegmann et al., 2018, Kretschmer et al., 2018, Meiji et al., 2008]. It is important to notice that during January, both HIYs and LIYs show an opposite pattern specially in Central Siberia were the anomalies are statistically significant. Also, a noticeable part of the southern Europe is influence by a statistically significant negative anomaly in December both during HIYs and LIYs. Finally, in February, there is a significant positive anomaly over most of the southern and eastern Europe in HIYs. However, such pattern is not observable in LIYs.

Interestingly, the European continent is more influenced (both in terms of frequency of the occurrence and the statistical significance of the impacted region) during HIYs than LIYs. Also, during the autumn season, the European continent experiences a statistically significant negative anomaly during September HIYs but not in any of the LIYs' months.

4.2.5 Precipitation

Screen [2013] studied the six summers from 2007 to 2012. The important features amongst these summers are that they were all wetter than average over northern Europe and they were six consecutive summers. Screen 2013 using composite and model analysis tried to find the impact of Arctic sea ice on European summer climate. It was found that these summer months tend to occur when the jet stream (300 hPa) is shifted to the south of its climatological location. Also, using simulation, it is found that the resulting shift in the jet stream is the direct consequence of Arctic sea ice loss. Cherenkova and Semenov [2017] in a separate study tried to investigate the spatial and temporal like between the winter precipitation variability and variations in the North Atlantic sea surface temperature, the Arctic sea ice concentration, and 500 hPa geopotential height in the Northern Hemisphere is analyzed for the period of 19522012. They found that the north Atlantic oscillation (NAO) can explain most of the observed connection between the studied parameters while the Atlantic multidecadal oscillation (AMO) explains the winter precipitation anomalies during years with the same sing as AMO with maximum anomaly over the east European plain and Balkan region.

In this section, a closer look at total precipitation (i.e. rain and snow) is taken. Figure

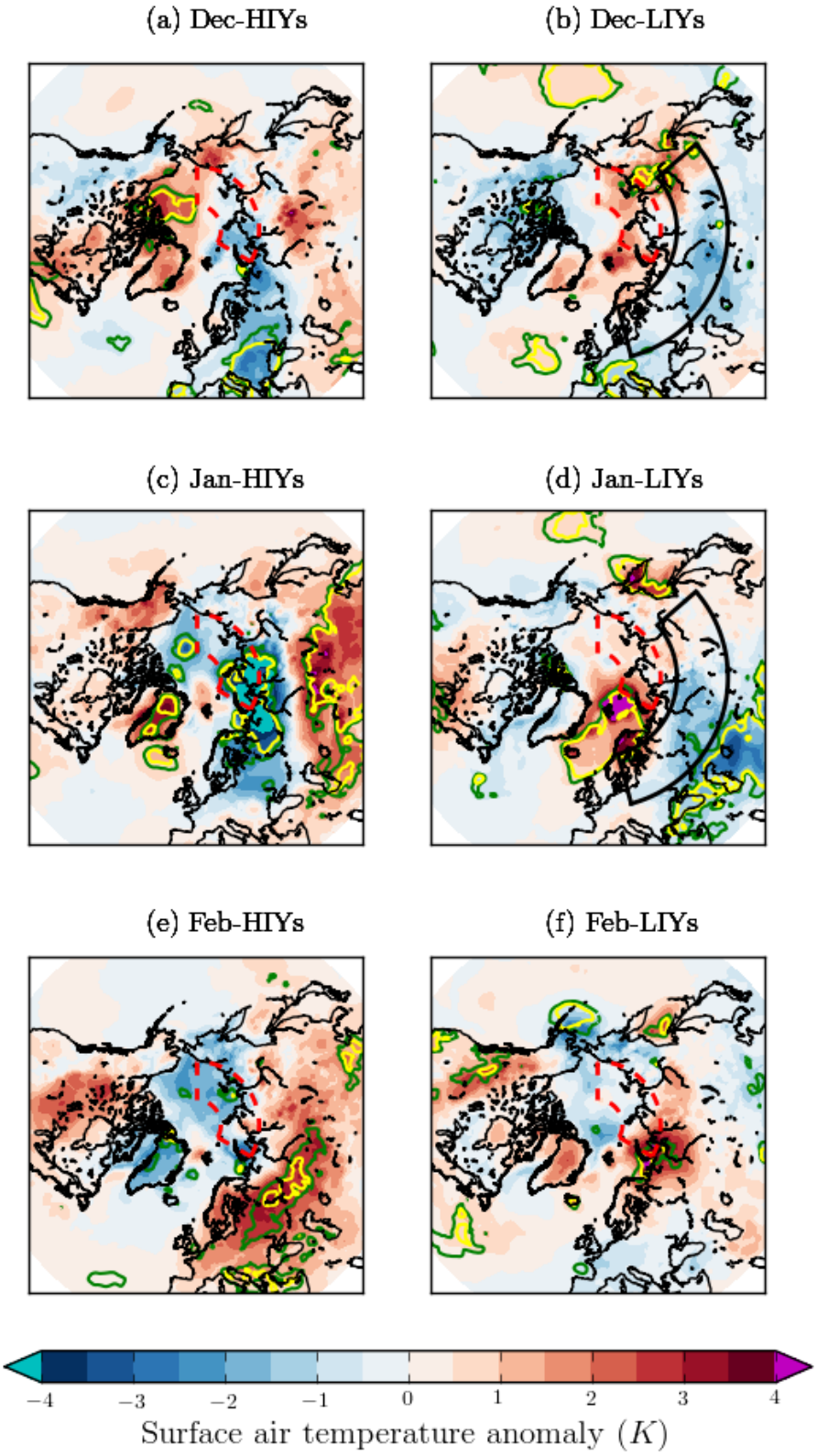

Figure 15: Winter SAT anomaly northward of 40 latitude. Solid Green, Yellow and dashed red lines are similar to Fig. 11. The area enclosed by the black sold line shows the cold part of the WACS pattern during LIYs in December and January (coordinates were taken from Fig. 7 of Kretschmer et al. [2018]). There is a statistically significant negative anomaly over southern Europe in both LIYs and HIYS during December. During January HIYs, northern Eurasia shows a significant negative anomaly. A pattern well observed during winter time.

16 shows the total precipitation anomaly during September, October, January, and February. Interestingly, all HIYs' months except October, show a statistically significant positive anomaly over Europe and Eurasia while of the all LIYs' months only October shows a significant anomaly where it is located over KSS. The positive and negative anomalies over Europe and off the coast of Norway and the UK during September HIYs and LIYs are possibly due to atmospheric circulations. Considering Fig. 18-a, there is one statistically significant high pressure system over northern Scandinavia and one low pressure system over central Europe. The two observed negative precipitation regions off the coast of Norway and the UK are the direct result of this high pressure system while the positive precipitation anomaly over central Europe is possibly the result of interaction between the high and low pressure systems. The low pressure system brings in the warm air from inland while the high pressure system brings in the cool air from the ocean and they meet over central Europe. Also, Fig. 12-a shows a strong convergence of latent energy over this region. Nevertheless, given the fact that during September the temperature gradient between land and ocean is not as large as what is seen in October and November, further analysis is required regarding the observed precipitation patterns during September.

The positive anomaly in October LIYs can be explained by connecting the results of the energy budget anomaly (Sec. 4.2), SST (Sec. 4.2.3), and water vapor (Sec. 4.2.1). Once the surface looses energy in latent form due to temperature gradient between ocean and atmosphere (Fig. 11-d and 14-d), the resulting evaporation forms a positive water vapor anomaly over this region (Fig. 12-d). Eventually, this water vapor falls in the form of precipitation. Contrary to this explanation, looking at Fig. 13-d the positive cloud anomaly over KSS does not cover a wide area similar to what is seen in Fig. 16-d.

Figure 16-e shows a strong positive anomaly over the central Siberia where the WACS happens (see Sec.4.2.4 and Fig. 15). Looking at Fig. 19-c it is clear that there exist a large anomalous low pressure system that resembles the precipitation pattern very well (extended from central Siberia toward north east Siberia and the sea of Japan). Also, given the extension of this low pressure system and the fact that it has a cyclonic motion, it is very likely that part of the water vapor required for the observed precipitation pattern originates from the sea of Japan. Looking at latent energy anomaly map in winter season, two statistically significant convergence anomalies are extended over the same area (central Siberia to the sea of Japan), however, they are not big in terms of area they cover. It appears that there is a connection between the sea of Japan and the precipitation in central and north east Siberia. However, further analysis is required to find a better picture of the mechanisms in action.

Finally, Fig. 16-g shows a large area of statistically significant positive anomaly over northern and central Europe. This anomaly, also, can be explained by the presence of a sizeable low pressure system over the same region (Fig. 19-e). Similarly, a close inspection of the latent energy anomaly map of the February HIYs (not shown) reveals that there is a convergence anomaly over the same region, however, only a small portion of this anomaly is statistically significant at 90 percent.

4.2.6 Dry Static and Latent Energy

Recently, atmospheric heat transport (AHT) and its contribution to the Arctic weather pattern has attracted more attention [Kjellsson, 2015, Yang et al., 2015, Yang and Dai, 2015]. It has been suggested that anomalously high AHT to the Arctic region can have significant impact on the SIC [G. and Mattias, 2016, Graversen et al., 2011]. Generally, AHT is composed of two components; dry static and latent where the latter is linked to water vapor (see Sec 4.2.1). Also, it has been found that the latent component of the AHT has a more pronounced role in sea ice loss process in the Arctic region [Kapsch et al., 2013].

G. and Mattias [2016] investigated the meridional energy transport of planetary and synoptic-scale waves to the Arctic region using a Fourier decomposition method which differentiates the contribution of each wave based on zonal wave numbers (i.e. zonal length-scales). They find that energy transport by planetary waves is considerably higher than the contribution of the synoptic waves. Also, they find that the latent energy transported by both planetary and synoptic-scale waves has more impact on the Arctic than the dry static energy transported by these systems. In a different study, Yang et al. [2015], using a coupled climate model (CESM1.0), studied AHT in detail. They find that in the extratropics both dry and latent energy are poleward and strengthen one another. Also, they find that the eddy components are the driving force behind the dry and latent energies.

Figure **??** shows the smoothed vertically integrated latent energy divergence and convergence anomaly over Europe and KSS northward of 40 ◦ latitude. It is evident that in September during HIYs there is a statistically significant energy convergence over Europe while in the same month during LIYs there is a significant energy divergence anomaly off the western coast of the UK (Fig. 17-a and b. The considerable convergence of the latent energy over Europe indicates that there has to be a mechanism that brings about the convergence over this region and atmospheric circulations are probably the most likely mechanisms. A close look at the KSS during September LIYs shows that there is no significant anomaly over this region Fig. 17-d. On the other hand, a statistically significant positive anomaly is observable

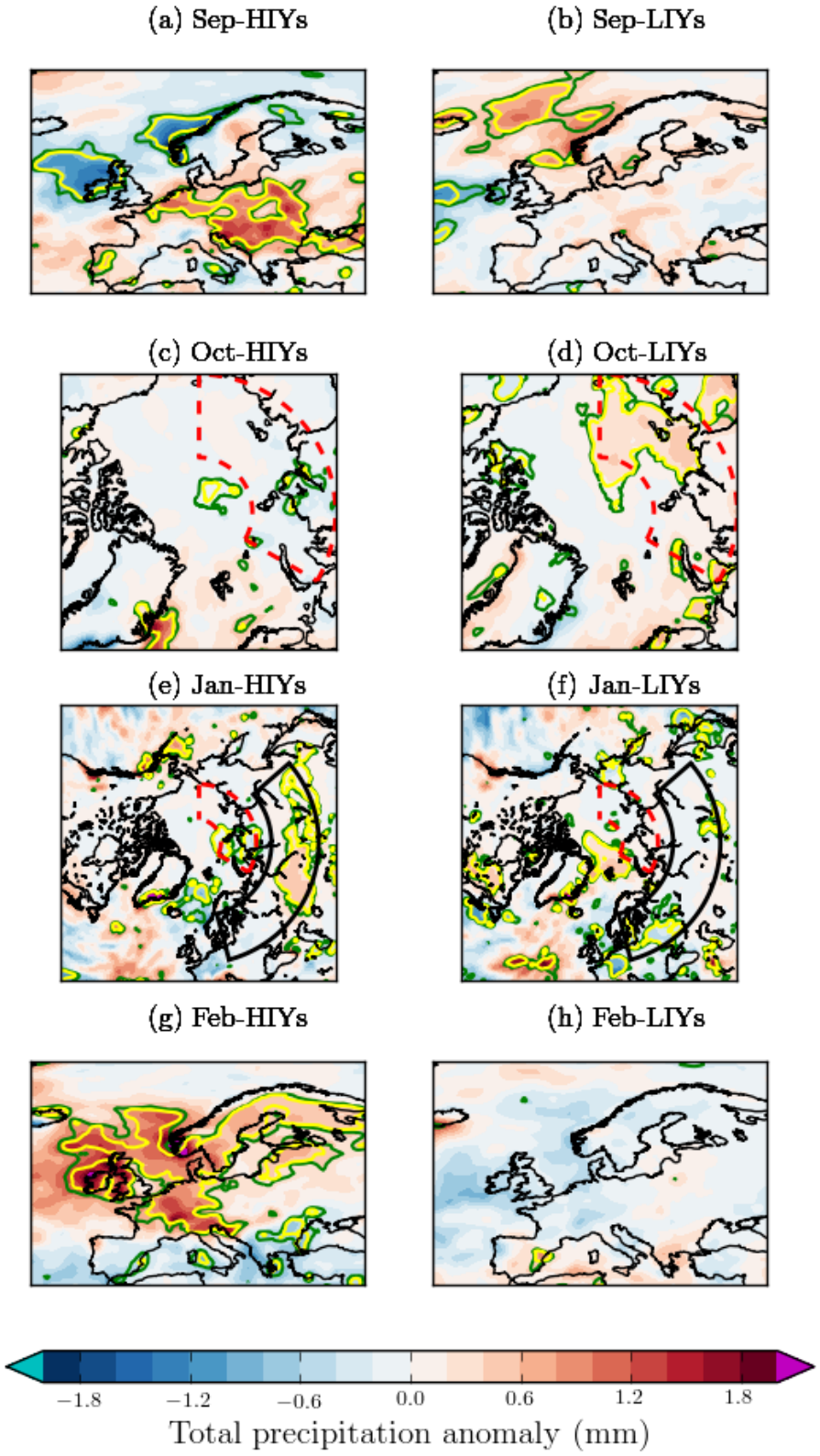

Figure 16: Total precipitation anomaly over Europe (rectangles) and the KSS (squares; dashed red line) during September, October, January, and February. Notice that only regions with strong anomalies (along with their counter plot) are shown during each month. The black solid line in (e) and (f) indicates the central Siberia where the WACS happens (see Fig. 15-c or -d and Sec. 4.2.4 for more details). There is a strong positive anomaly over Europe both in September and February HIYs.

over the Barents sea in September during HIYs (Fig. 17-c). It is very probable that the anomalous latent energy divergence over the Barents sea is the result of two connected mechanisms, namely anomalously positive SST and atmospheric circulation (see Fig. 14 for SST and Sec. 4.2.7 on atmospheric circulation). Also, given the fact that latent energy is associated with water vapor, the observed positive anomaly of the latent energy can result in lack of moisture and, accordingly, CC in the atmosphere. This can possibly explain the anomalously low CC over this region during the same month and period (i.e. HIYs; Fig. 13-a).

During November HIYs only a significantly positive anomaly is observable over the western coast of Portugal (Fig. 17). This pattern is not unexpected since this area is the center of a statistically significant high pressure system during the same period (Fig. 17-e and Fig. 18-e). A similar pattern can be seen in November but this time during LIYs (Fig. 17-f). Also, a small but statistically significant convergent region of latent energy is located on the northern coast of Norway. Both patterns are results of the anomalously high and low pressure system on these regions respectively (18-e and Fig. 18-f).

Finally, in the KSS region, in November HIYs there is very little anomaly on this region, however, most of the Barents sea shows a statistically significant convergence anomaly Fig. 17-g. This behavior is possibly the direct result of the anomalous high pressure system over this region (18-e). Interestingly, in November LIYs there is a small but statistically significant divergent behavior in latent energy over KSS, however, this time there is no center of low or high pressure system over this region (Fig. 17-h and Fig. 18-f). Nevertheless, this pattern can possibly be explained by the atmospheric circulation at this region. Given the atmospheric circulation over this area, and the temperature gradient between ocean and continent in this month, it is likely that the cold, dry air from northern Siberia dominates the warm, moist air from the northern Atlantic over the KSS. The dominance of the cold, dry air over the KSS result and the warmer than usual temperature of the surface at the same area result in anomalous cooling of the surface during November LIYs (Fig. 9, Fig. 14-f and Fig. 11-d)

4.2.7 Atmospheric Circulation

Generally, atmospheric circulation and sea ice influence one another through a feedback cycle with many dynamical and thermodynamical factors involved. In this section an attempt will be made to investigate the possibility of any atmospheric circulation anomalies and the likely reasons behind them at SLP, lower (850 hPa), middle (500 hPa). Finally, stratospheric polar

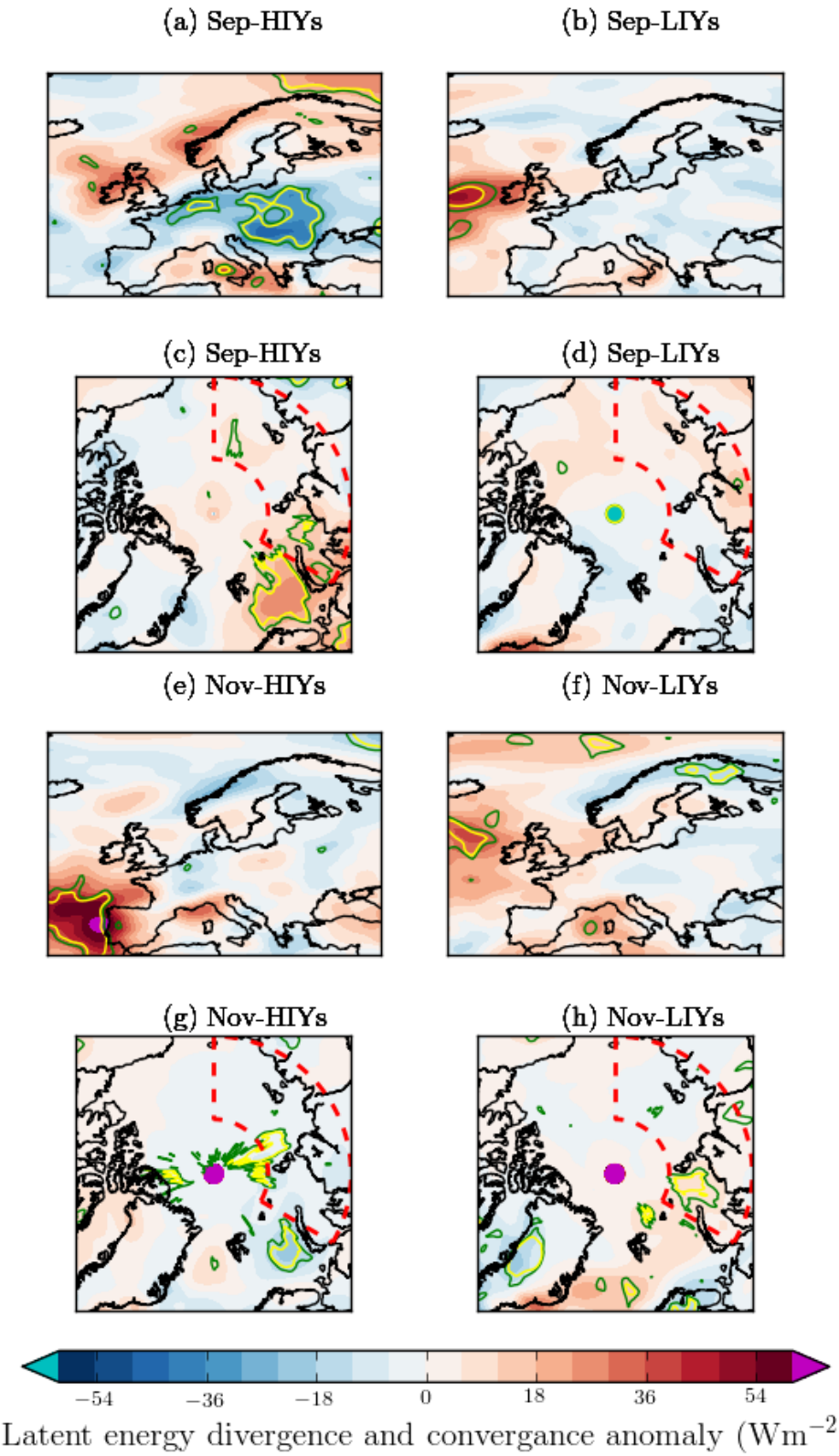

Figure 17: Smoothed vertically integrated latent energy divergence and convergence anomaly over Europe and KSS. Notice that only September and November anomalies are shown. Also, no significant anomaly was observed over Eurasia during any of the HIYs and LIYs.

vortex (10 hPa) anomaly will be discussed briefly.

4.2.8 Sea Level Pressure and Lower Troposphere Circulation

Studies have shown that close-to-surface atmospheric circulations can dynamically impact SIC by exerting force on sea ice pieces and moving them in or out of the Arctic region [Masayo and M., 2007]. For instance, Masayo and M. [2012] studied the yearly and multidecadal variability of SIC using 925 hPa wind anomalies. They find that winters preceding years with low September SIC show a higher rate of sea ice flow out of the Arctic region through Fram strait. Also, they find that the combined effect of winter and summer wind forcing accounts for ~ 50 % yearly and ~ 30 % of 31 year-interval (1979-2009) ice variability in the Arctic region respectively.

Zhao et al. [2018] focused on the role of wind forcing on what they call CARLIC (record low ice concentration in the central Arctic) during the Summer of 2010. Using wind stress curl, they suggest that regional wind forcing may have played a key role in ice loss process compared to ice melt due to solar radiation in Summer 2010. However, they also argue that despite large wind stress curls during 2003 and 2006, the CARLIC was not observed (unlike 2007 and 2010). They argue that the presence of heavy multiyear ice in 2003 and 2006 prevented the wind forcing from formation of ice drift divergence as is the case for regions with thin and first-year ice coverage.

Figure 18 shows several significant anomalies in SLP over KSS and Europe. Looking at September LIYs (Fig. 18-b), the position of negative anomaly over the Bering strait and the positive anomaly over the north pole may contribute to the observed positive anomaly of SST over the Chukchi sea in September LIYs (see Fig. 14). It is well known that an air mass around low and high pressure systems rotates cyclonically and anti-cyclonically respectively (see Sec. 2 for further details on air flow around high and low pressure systems). In that regard, it is possible that the observed positive SST anomaly at September LIYs is the result of wind forcing due to SLP configuration (see LIYs September atmospheric circulation in Fig. 18-b and 20-b).

SLP anomaly in October LIYs (Fig. 18-d) shows a statistically significant negative anomaly over KSS. This behavior is likely the direct result of the considerable amount of energy flux from the KSS to the atmosphere above during this time (Fig. 10) where this energy flux is a consequence of anomalously low or thin ice cover at KSS. The ice anomaly during October LIYs, exposes water to the atmosphere and the energy exchange process accelerates. Although statistically not significant, but the negative anomaly is still present in 850 hPa

pressure level (Fig. 20-d). This negative anomaly is only slightly present in November, which is not unexpected, since the flux anomaly and total energy component plots do not show strong anomalies. A close look at the October and November anomalies in both SLP and 850 geopotential height in HIYs does not show any statistically significant anomaly over the KSS (Fig. 18-c,e and Fig. 20-c,e). This lack of strong anomalies over KSS is likely due to the fact that there is no strong anomaly in energy budget of the surface during these months in HIYS.

4.2.9 Middle Troposphere Circulation

Pedersen et al. [2016], explore the impact of three different scenarios of sea ice loss (over the entire Arctic, Atlantic and Pacific sections) on atmospheric circulation using a general circulation model. They find that in all three models the 500 hPa geopotential height increases near the sea ice loss area due to transfer of heat flux from ocean to the atmosphere. They, also, find that considerable surface warming is possible without notable increase in geopotential height above. However, they do not find any direct relation between the spatial pattern of the warming region and the 500 hPa geopotential height. Also, they find that as a result of increased geopotential height in the Arctic region the temperature gradient between the Arctic and lower latitudes decreases which in turn leads to slower zonal winds and more persistent weather patterns at lower latitudes.

In order to investigate the possible impact of middle troposphere on lower troposphere and surface, the 500 hPa gepotential height anomaly map was plotted (Fig. 21). A noticeable feature of the 500 mb anomaly plot is the negative significant anomaly in October during LIYs over the KSS (Fig. 21-d). To take a closer look at this anomaly at both 500 and 850 mb, a thickness plot was made (Fig. 22-a and b). Both 850-1000 and 500-1000 mb thickness levels show a statistically significant anomalous behavior during September HIYs and LIYs. Unlike LIYs, during HIYs both levels show a sharp increase in the height of thickness from September to November with its peak in November. Interestingly, during October LIYs at both levels there is no significantly anomalous behavior. The possible interpretation of this lack of statistically insignificant anomaly is twofold: the increase in the height of 1000, 850, 500 mb pressure levels has been nearly similar and the fact that these results are the outcome of an area weighted thickness anomaly and looking at Fig. 20-d and Fig. 21-d no area and only a small area over the KSS show statistically significant anomaly respectively.

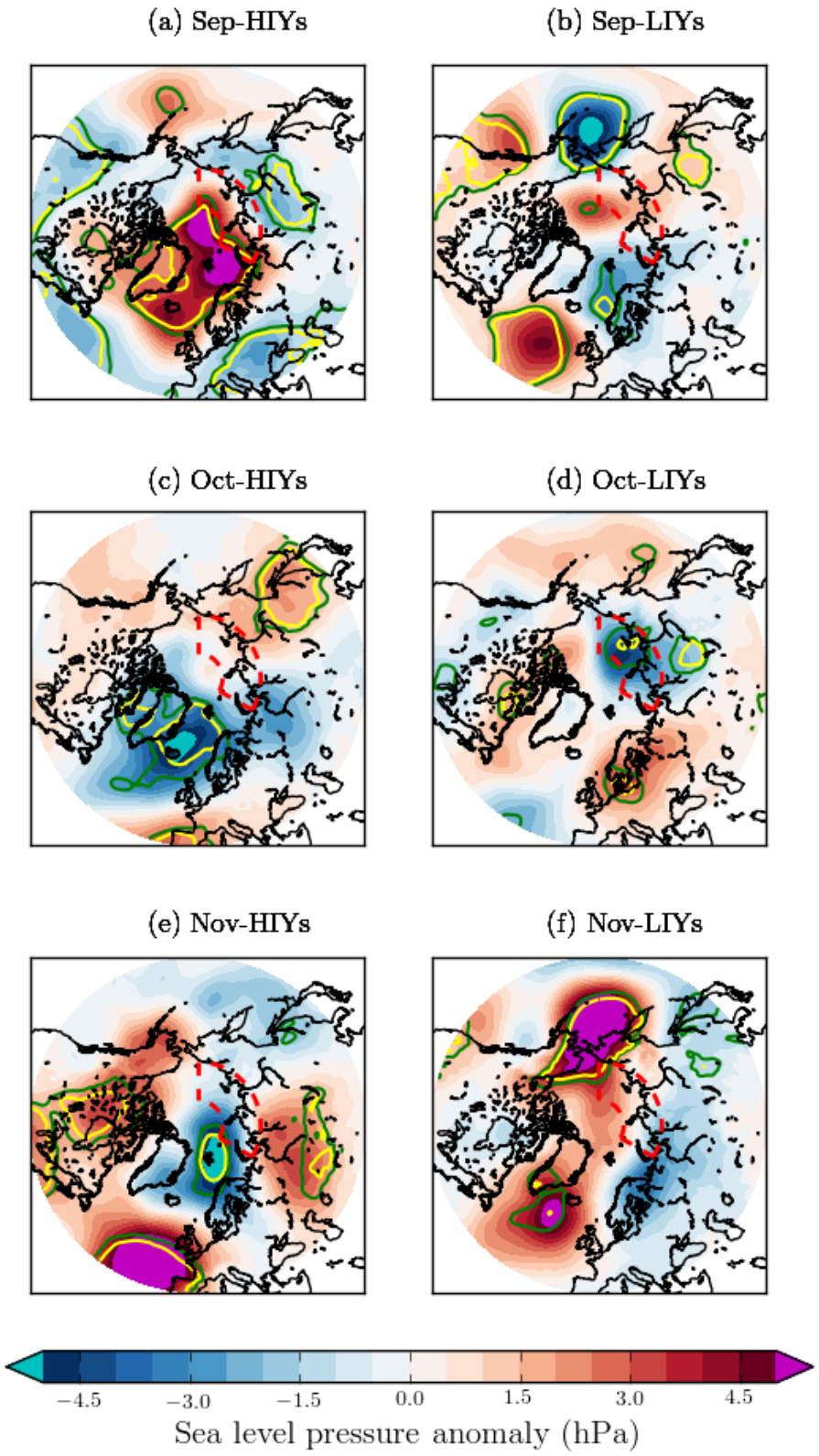

Figure 18: Sea level pressure anomaly northward of 40 latitude. Kss is enclosed with dashed red line. The green and yellow solid lines show the statistical significance of 90 and 95 percent respectively. There several strong anomalies both over the KSS and Europe. The apparent anomaly over KSS in October is clear.

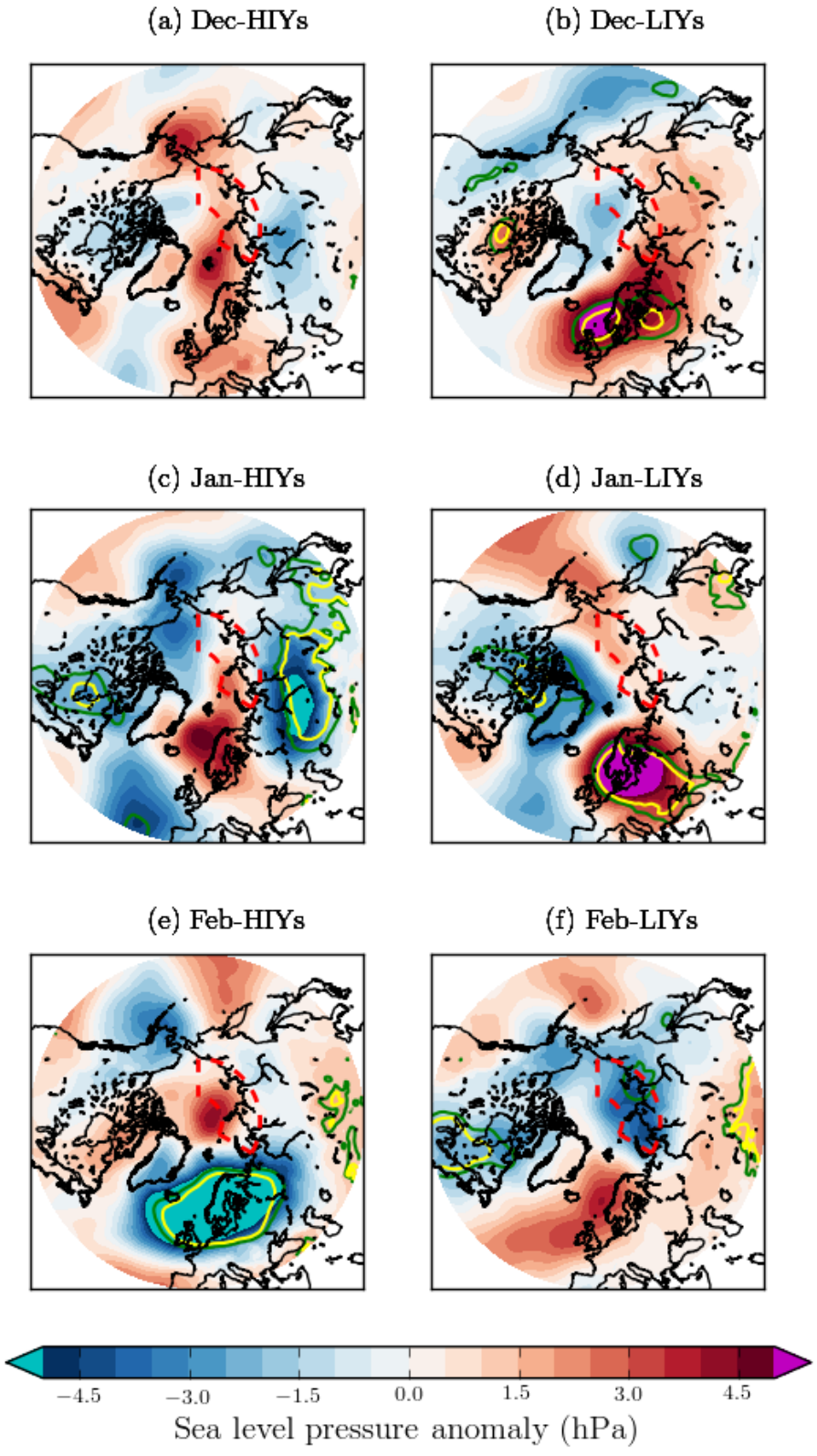

Figure 19: Similar to Fig. 18 but for winter season (December, January, February).

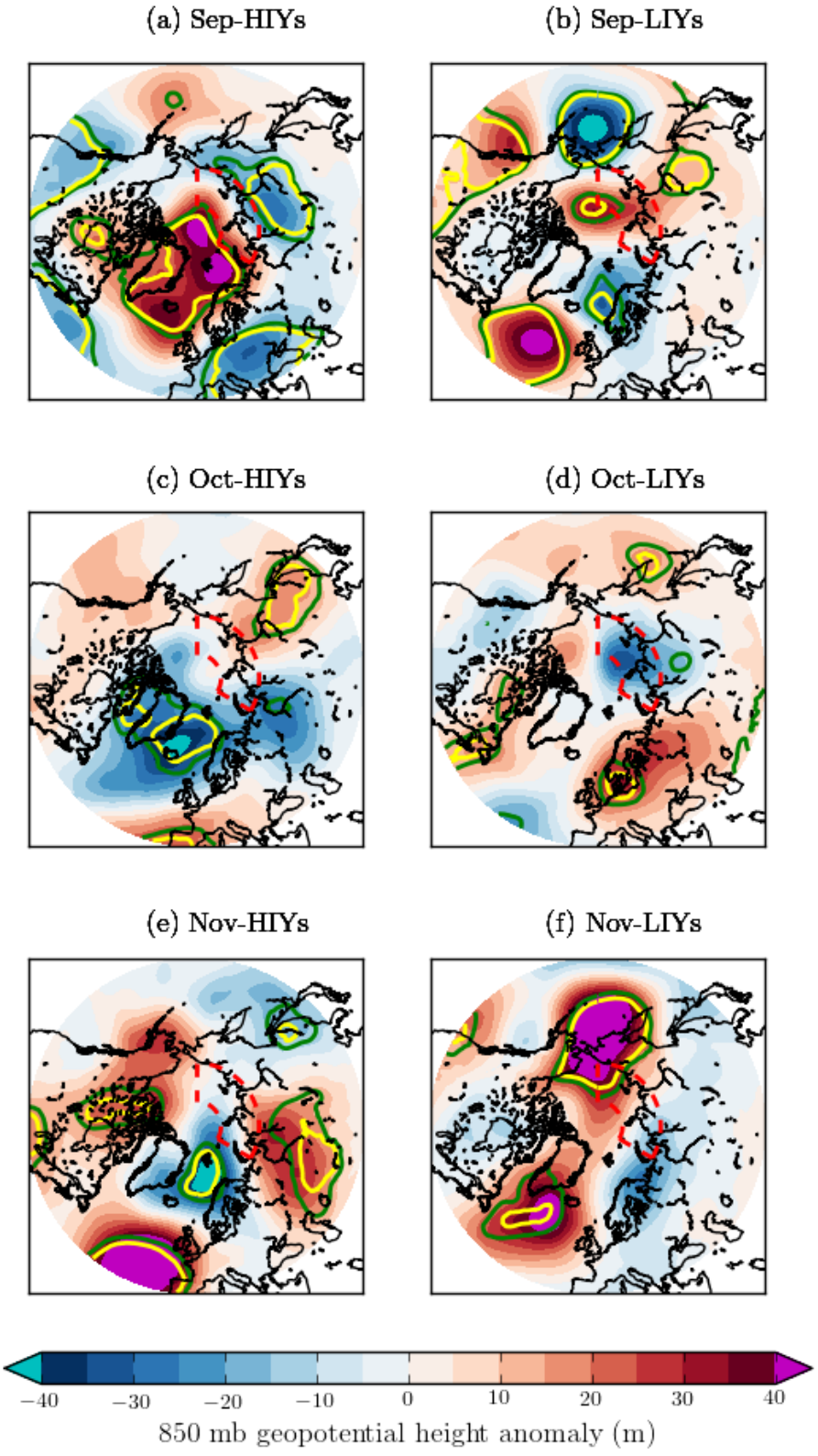

Figure 20: 850 mb geopotential height anomaly northward of 40 latitude. The green and yellow solid lines show the statistical significance of 90 and 95 percent respectively. There several strong anomalies both over the KSS and Europe. The anomaly over KSS in October during LIYs is still visible, however,it is not statistically significant.

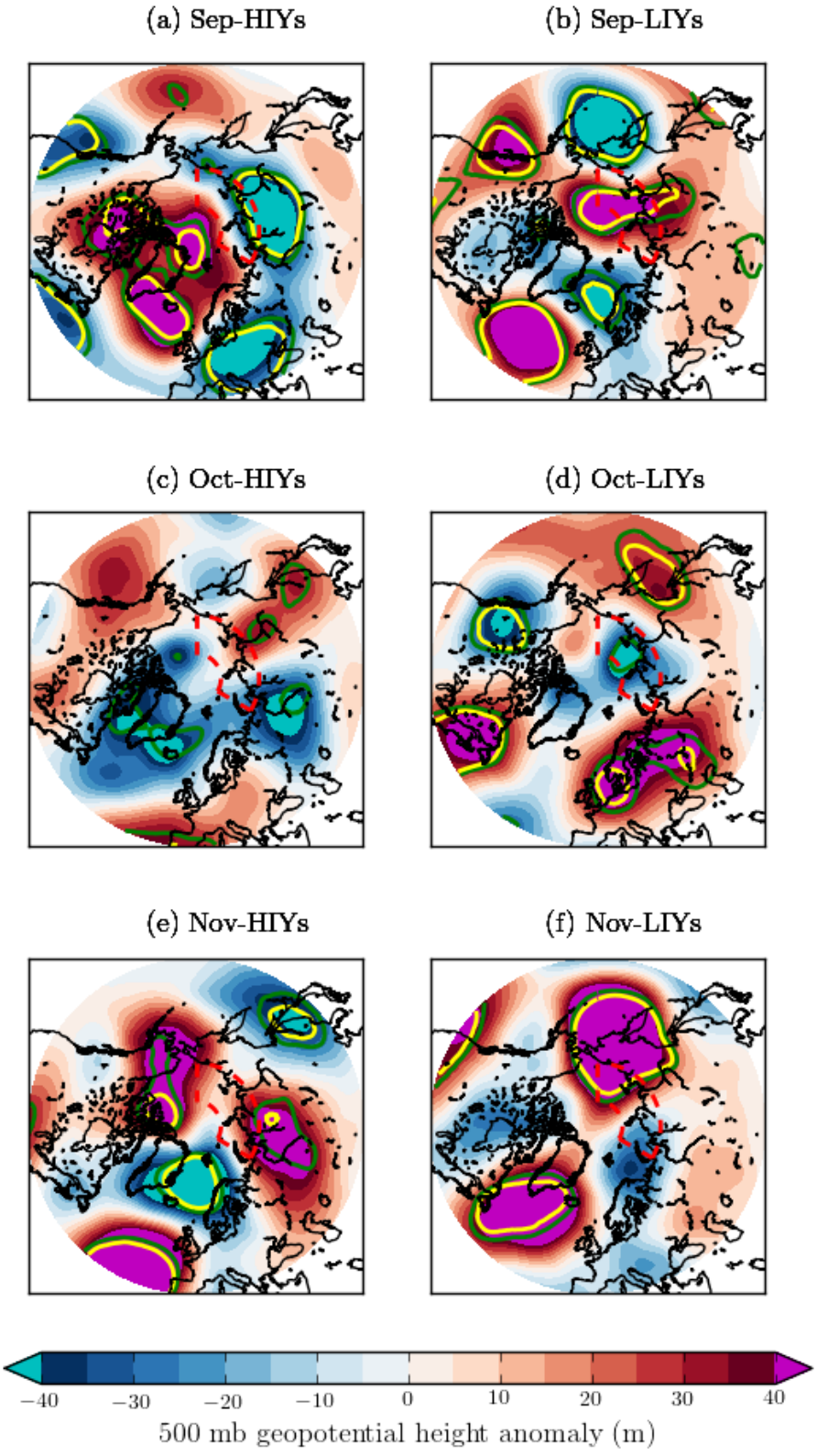

Figure 21: 500 mb geopotential height anomaly northward of 40 latitude. The green and yellow solid lines show the statistical significance of 90 and 95 percent respectively. There are several strong anomalies both over the KSS and Europe. The anomaly over KSS in LIYs has become significant again in October.

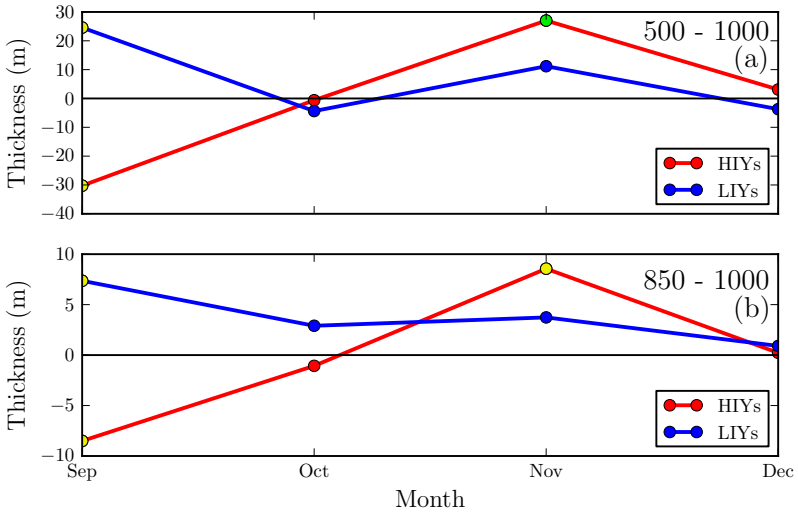

Figure 22: Area weighted 500-1000 (top) and 850-1000 mb (bottom) thickness anomaly over the KSS. The red and blue solid lines show the thickness in HIYs and LIYs respectively. The green and yellow circles show the statistical significance of 90 and 95 percent respectively (notice the yellow circles in September). The thickness shows a statistically significant low value during September HIYs at both plots, however, the thickness follows a sharp increase toward November with an anomalous peak in November. It is evident that the thickness during October does not show any statistically significant anomaly.

4.2.10 Stratospheric Polar vortex

Several studies have suggested a connection between the weak/strong state of the polar vortex and the extreme weather patterns observed in mid-latitudes [Kretschmer et al., 2018, Hu et al., 2018, Kretschmer et al., 2016]. Kretschmer et al. [2018], in a recent study, by applying clustering analysis on the daily mean zonal wind velocity field poleward of 60∘N at 10 hPa during January and February, suggested that a shift in polar vortex toward its weak states as the possible reason behind the unusually cold winters over Eurasia.

Similar to Kretschmer et al. [2018], the 10 hPa geopotential height was chosen as the stratospheric polar vortex pressure level. Figure 23 shows the polar vortex anomalies northward of 40∘N for autumn. It is evident that September HIYs, November HIYs, and October LIYs all show a strong dipole pattern over the Arctic region. This pattern has been suggested as the weak state of the polar vortex and has been associated with the observed cold winter pattern over Eurasia (see Fig. 1 in [Kretschmer et al., 2018]).

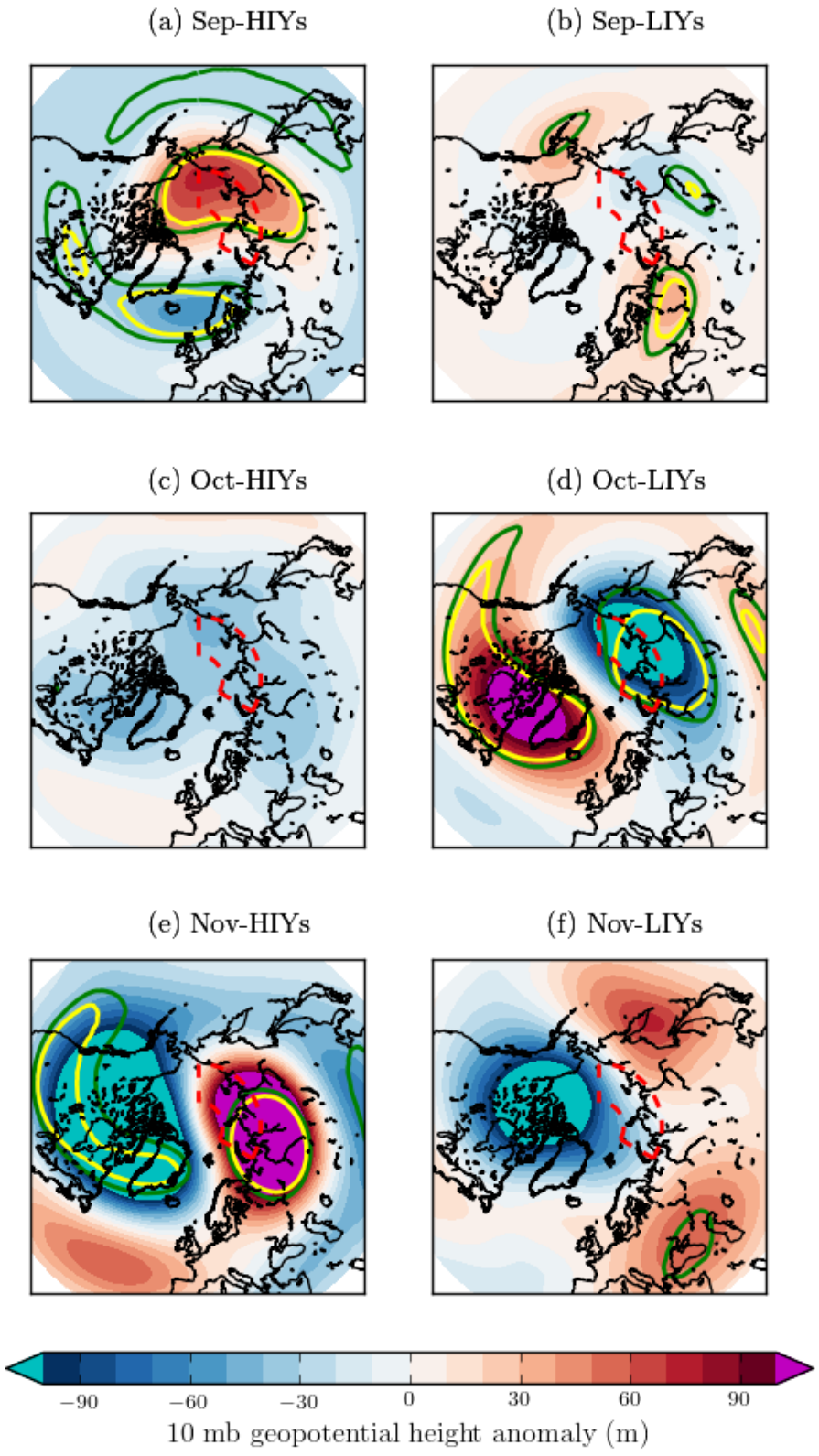

Figure 23: 10 mb geopotential height anomaly northward of 40 latitude. The green and yellow solid lines show the statistical significance of 90 and 95 percent respectively. A strong dipole pattern is evident in September HIYs, November HIYs, and October LIYs. Notice that the colorbar is scaled differently from the other geopotential heights.

5 Discussion and Conclusion

The behavior of several atmospheric parameters over Europe and Eurasia were compared during twp periods of HIYs and LIYs of the KSS. An anomalous behavior was observed for some of these parameters. Here, a short summary of the important findings of this study will be presented and a possible mechanism behind the observed behavior will be presented.

A statistically significant negative anomaly was observed in the behavior of the energy budget at the surface during October of the LIYs. A sign of anomalous loss of energy by the surface to the atmosphere above (Fig. 10 and 11-d). It appears that the anomalous loss of energy happens at the east Siberian sea rather than the Kara sea.

Similar to energy budget, water vapor shows an anomalous behavior at 1000 hPa over the east Siberian sea during October LIYs (Fig. 12). However, there is no anomalous behavior during the same period and region at 850 hPa.

Conversely, there is no statistically significant cloud formation over the KSS during October LIYs (Fig. 13-d). This is not consistent with the energy budget and water vapor behavior.

SST, also, shows a statistically significant anomalous behavior over the east Siberian sea during September and October LIYs (Fig. 14-b,d).

SAT shows the WACS pattern during both December and January LIYs while the same months in HIYs do not show a similar pattern (Fig. 15-b,d).

Precipitation does not show a statistically significant behavior over Europe or Eurasia during LIYs (only a positive anomaly over KSS). On the other hand, there are several positive anomaly over Europe and Eurasia during September, January, and February HIYs (Fig. 16).

Latent energy only shows a statistically convergent behavior over Europe during September where it is consistent with the anomalous behavior of the precipitation during September HIYs. Also, there is a strong divergent behavior of the latent energy near the western coast of Spain ans Portugal (Fig. 17).

Dry static energy does not show any statistically significant anomaly over Europe and Eurasia at a significance level of 90 and 95 percent (not shown).

SLP shows a statistically significant negative anomaly over the east Siberian sea at 90 percent significance level (Fig. 18-d).

Geopotential height at 850 hPa does not show a statistically significant behavior over the

KSS while the 500 hPa geopotential height shows a statistically significant negative behavior at 90 percent significance level over east Siberian sea during October LIYs (Fig. 20-d and 21-d).

Similar to SLP and 500 hPa geopotential height, stratospheric polar vortex at 10 hPa shows a statistically significant negative anomaly at both 90 and 95 percent level over KSS during October LIYs (Fig. 23-d).

In order to put the above findings into a consistent frame, SST can be used as the starting point. During September and October the SST shows a statistically significant positive anomaly over the east Siberian sea. This positive anomaly is the result of the presence of warm water in this region. Further, it is likely that the intrusion of warm water through Bering strait into the east Siberian sea is the result of the atmospheric circulation in this region. Given the SLP pattern during September LIYs, there is a strong low pressure system over the Bering strait and a high pressure system close to the cap of the Arctic sea. Consequently, the cyclonic circulation of the low pressure system and anticyclonic circulation of the high pressure system results in the intrusion of the warm water into the east Siberian sea. The warm water in the east Siberian sea results in a substantial loss of sea ice in this region. Later during October LIYs, the east Siberian sea is exposed to the cold air above (Fig. 9) which results in an anomalous energy flux to the atmosphere. This probably explains the statistically significant negative anomaly of the energy budget over the east Siberian sea during October LIYs. Since the energy loss of the open water to the atmosphere is partially in the form of water vapor (water molecules with higher energy will be advected from the water to the cold atmosphere above) the anomalous behavior of the water vapor during October LIYs at 1000 hPa level can be explained by the anomalous advection of the water vapor to the atmosphere during October LIYs. The anomalous flux of energy to the atmosphere will disturb the atmospheric circulation at 850, 500, and 10 hPa by creating a statistically significant negative anomaly over the east Siberian sea, however, the process through which this negative anomaly is created is not fully understood and is out of the scope of this work. It is likely that the disturbance in the stratospheric polar vortex at 10 hPa later in the winter impacts the troposphere and, consequently, the surface by disturbing the atmospheric circulation. It is crucial to notice that the atmospheric parameter's behavior over Europe and Eurasia is statistically more significant and pronounced during HIYs than during LIYs. This is particularly clear in the precipitation pattern. There is a strong positive precipitation pattern during January HIYs over Eurasia and during February HIYs over Europe where it mostly effects the central and northern Europe. Considering the SLP anomalies, it is highly probable that the atmospheric circulation pattern during January and February HIYs

is the responsible mechanism behind the statistically significant positive anomaly of the precipitation over Europe and Eurasia. While during HIYs there are several strong anomalies during winter, there is no statistically significant behavior in the precipitation pattern over Europe and Eurasia during LIYs. Finally, SAT shows anomalous behavior over Europe and Eurasia during both HIYs and LIYs, however, the WACS pattern is present, only, during December and January of the LIYs. Looking at SLP pattern during December can explain the WACS pattern during the same month in LIYs. The low pressure system over the cap of the Arctic region brings in the warm humid air from the ocean to the KSS region through cyclonic motion while the high pressure system extended from the northern Europe to the east Siberia and Japan can bring in cold air from the east end of the Siberia to the central Siberia and Eurasia through an anti cyclonic air flow. While January LIYs shows a WACS pattern, it is hard to explain the observed behavior solely based on the SLP pattern and it needs further investigation.

This study shows that the SST can play a significant role in the sea ice loss process in the east Siberian sea and further disturbing the atmospheric circulation over the same region. Also, it was found that the east Siberian section of the Arctic ocean plays an important role in disturbing the atmospheric circulation compared to the Kara sea. Also, the study shows that precipitation increases during the HIYs compared to LIYs. In addition, it was found that while both LIYs ans HIYs show statistically significant anomalies of the SAT, the WACS pattern is only observed during LIYs. Dry static energy shows no significant behavior at 90 and 95 percent level significance while latent energy show some statistically significant convergent behavior over Europe during September HIYs. Finally, it was shown that the atmospheric circulation at 500 hPa and stratospheric polar vortex (10 hPa) are significantly disturbed over the east Siberian and KSS respectively during October LIYs.

References

Woodgate Rebecca A., Weingartner Tom, and Lindsay Ron. The 2007 bering strait oceanic heat flux and anomalous arctic seaice retreat. *Geophysical Research Letters*, 37(1), 2009. doi: 10.1029/2009GL041621. URL https://agupubs.onlinelibrary.wiley.com/doi/abs/10.1029/2009GL041621.

Stefanie Arndt. Sea-ice surface properties and their impact on the under-ice light field from remote sensing data and in-situ measurements. *Doctoral Thesis*, Nov 2016.

Yunfeng Cao, Shunlin Liang, Xiaona Chen, Tao He, Dongdong Wang, and Xiao Cheng. Enhanced wintertime greenhouse effect reinforcing arctic amplification and initial sea-ice melting. *Scientific Reports*, 7, Aug 2017. doi: 10.1038/s41598-017-08545-2. URL https://doi.org/10.1038/s41598-017-08545-2.

D. J. Cavalieri and C. L. Parkinson. Arctic sea ice variability and trends, 1979,2010. *The Cryosphere*, 6(4):881–889, 2012. doi: 10.5194/tc-6-881-2012. URL https://www.the-cryosphere.net/6/881/2012/.

Ping Chen and Jinping Zhao. Variation of sea ice extent in different regions of the arctic ocean. *Acta Oceanologica Sinica*, 36(8):9–19, Aug 2017. ISSN 1869-1099. doi: 10.1007/s13131-016-0886-x. URL https://doi.org/10.1007/s13131-016-0886-x.

E. A. Cherenkova and V. A. Semenov. A link between winter precipitation in europe and the arctic sea ice, sea surface temperature, and atmospheric circulation. *Russian Meteorology and Hydrology*, 42(4):238–247, Apr 2017. doi: 10.3103/S1068373917040045. URL https://doi.org/10.3103/S1068373917040045.

Judah Cohen. An observational analysis: Tropical relative to arctic influence on mid-latitude weather in the era of arctic amplification. *Geophysical Research Letters*, 43(10):5287–5294, 5 2016. ISSN 1944-8007. doi: 10.1002/2016GL069102. URL http:https://doi.org/10.1002/2016GL069102.

Judah Cohen, James A. Screen, Jason C. Furtado, Mathew Barlow, David Whittleston, Dim Coumou, Jennifer Francis, Klaus Dethloff, Dara Entekhabi, James Overland, and Justin Jones. Recent arctic amplification and extreme mid-latitude weather. *Nature Climate Change*, 7, Aug 2014. doi: 10.1038/ngeo2234. URL http://dx.doi.org/10.1038/ngeo2234.

Peter E. D. Davis, Camille Lique, Helen L. Johnson, and John D. Guthrie. Competing effects of elevated vertical mixing and increased freshwater input on the stratification and sea ice

cover in a changing arctic ocean. *Journal of Physical Oceanography*, 46(5):1531–1553, 2016. doi: 10.1175/JPO-D-15-0174.1. URL https://doi.org/10.1175/JPO-D-15-0174.1.

Dee, Uppala S. M., Simmons A. J., Berrisford P., Poli P., Kobayashi S., Andrae U., Balmaseda M. A., Balsamo G., Bauer P., Bechtold P., Beljaars A. C. M., van de Berg L., Bidlot J., Bormann N., Delsol C., Dragani R., Fuentes M., Geer A. J., Haimberger L., Healy S. B., Hersbach H., Hlm E. V., Isaksen L., Kllberg P., Khler M., Matricardi M., McNally A. P., MongeSanz B. M., Morcrette J.J., Park B.K., Peubey C., de Rosnay P., Tavolato C., Thpaut J.N., and Vitart F. The erainterim reanalysis: configuration and performance of the data assimilation system. *Quarterly Journal of the Royal Meteorological Society*, 137(656):553–597, 2011. doi: 10.1002/qj.828. URL https://rmets.onlinelibrary.wiley.com/doi/abs/10.1002/qj.828.

Jennifer A. Francis and Stephen J. Vavrus. Evidence linking arctic amplification to extreme weather in midlatitudes. *Geophysical Research Letters*, 39(6), 3 2012. ISSN 1944-8007. doi: 10.1029/2012GL051000. URL http:https://doi.org/10.1029/2012GL051000.

Jennifer A Francis and Stephen J Vavrus. Evidence for a wavier jet stream in response to rapid arctic warming. *Environmental Research Letters*, 10(1):014005, 2015. URL http://stacks.iop.org/1748-9326/10/i=1/a=014005.

Ogawa Fumiaki, Keenlyside Noel, Gao Yongqi, Koenigk Torben, Yang Shuting, Suo Lingling, Wang Tao, Gastineau Guillaume, Nakamura Tetsu, Cheung Ho Nam, Omrani NourEddine, Ukita Jinro, and Semenov Vladimir. Evaluating impacts of recent arctic sea ice loss on the northern hemisphere winter climate change. *Geophysical Research Letters*, 45(7):3255–3263, 2017. doi: 10.1002/2017GL076502. URL https://agupubs.onlinelibrary.wiley.com/doi/abs/10.1002/2017GL076502.

Graversen Rune G. and Burtu Mattias. Arctic amplification enhanced by latent energy transport of atmospheric planetary waves. *Quarterly Journal of the Royal Meteorological Society*, 142(698):2046–2054, 2016. doi: 10.1002/qj.2802. URL https://rmets.onlinelibrary.wiley.com/doi/abs/10.1002/qj.2802.

Rune G. Graversen, Thorsten Mauritsen, Sybren Drijfhout, Michael Tjernström, and Sebastian Mårtensson. Warm winds from the pacific caused extensive arctic sea-ice melt in summer 2007. *Climate Dynamics*, 36(11):2103–2112, Jun 2011. ISSN 1432-0894. doi: 10.1007/s00382-010-0809-z. URL https://doi.org/10.1007/s00382-010-0809-z.

Masatake E. Hori, Jun Inoue, Takashi Kikuchi, Meiji Honda, and Yoshihiro Tachibana. Recurrence of intraseasonal cold air outbreak during the 2009/2010 winter in japan and

its ties to the atmospheric condition over the barents-kara sea. *SOLA*, 7:25–28, 2011. doi: 10.2151/sola.2011-007.

Dingzhu Hu, Zhaoyong Guan, Wenshou Tian, and Rongcai Ren. Recent strengthening of the stratospheric arctic vortex response to warming in the central north pacific. *Nature Climate Change*, 9, Apr 2018. doi: 10.1038/s41467-018-04138-3. URL https://doi.org/10.1038/s41467-018-04138-3.

Jun Inoue, Masatake E. Hori, and Koutarou Takaya. The role of barents sea ice in the wintertime cyclone track and emergence of a warm-arctic cold-siberian anomaly. *Journal of Climate*, 25(7):2561–2568, 2012. doi: 10.1175/JCLI-D-11-00449.1. URL https://doi.org/10.1175/JCLI-D-11-00449.1.

Sedlar Joseph and Tjernstrm Michael. Clouds, warm air, and a climate cooling signal over the summer arctic. *Geophysical Research Letters*, 44(2):1095–1103, 2016. doi: 10.1002/2016GL071959. URL https://agupubs.onlinelibrary.wiley.com/doi/abs/10.1002/2016GL071959.

Yano JunIchi and Ambaum Maarten H. P. Moist static energy: definition, reference constants, a conservation law and effects on buoyancy. *Quarterly Journal of the Royal Meteorological Society*, 143(708):2727–2734, 2017. doi: 10.1002/qj.3121. URL https://rmets.onlinelibrary.wiley.com/doi/abs/10.1002/qj.3121.

Lu K., Weingartner T., Danielson S., Winsor P., Dobbins E., Martini K., and Statscewich H. Lateral mixing across ice meltwater fronts of the chukchi sea shelf. *Geophysical Research Letters*, 42(16):6754–6761, 2015. doi: 10.1002/2015GL064967. URL https://agupubs.onlinelibrary.wiley.com/doi/abs/10.1002/2015GL064967.

Marie-Luise Kapsch, Rune Grand Graversen, and Michael Tjernstrm. Springtime atmospheric energy transport and the control of arctic summer sea-ice extent. *Nature Climate Change*, 3, Apr 2013. doi: 10.1038/nclimate1884. URL http://dx.doi.org/10.1038/nclimate1884.

Marie-Luise Kapsch, Rune Grand Graversen, Michael Tjernstrm, and Richard Bintanja. The effect of downwelling longwave and shortwave radiation on arctic summer sea ice. *Journal of Climate*, 29(3):1143–1159, 2016. doi: 10.1175/JCLI-D-15-0238.1. URL https://doi.org/10.1175/JCLI-D-15-0238.1.

Baek-Min Kim, Seok-Woo Son, Seung-Ki Min, Jee-Hoon Jeong, Seong-Joong Kim, Xiangdong Zhang, Taehyoun Shim, and Jin-Ho Yoon. Weakening of the stratospheric polar vor-

tex by arctic sea-ice loss. *Nature Climate Change*, 5, Sep 2014. doi: 10.1038/ncomms5646. URL http://dx.doi.org/10.1038/ncomms5646.

Hye-Mi Kim and Baek-Min Kim. Relative contributions of atmospheric energy transport and sea ice loss to the recent warm arctic winter. *Journal of Climate*, 30(18):7441–7450, 2017. doi: 10.1175/JCLI-D-17-0157.1. URL https://doi.org/10.1175/JCLI-D-17-0157.1.

Martin P. King, Momme Hell, and Noel Keenlyside. Investigation of the atmospheric mechanisms related to the autumn sea ice and winter circulation link in the northern hemisphere. *Climate Dynamics*, 46(3):1185–1195, Feb 2016. ISSN 1432-0894. doi: 10.1007/s00382-015-2639-5. URL https://doi.org/10.1007/s00382-015-2639-5.

Joakim Kjellsson. Weakening of the global atmospheric circulation with global warming. *Climate Dynamics*, 45(3):975–988, Aug 2015. ISSN 1432-0894. doi: 10.1007/s00382-014-2337-8. URL https://doi.org/10.1007/s00382-014-2337-8.

Marlene Kretschmer, Dim Coumou, Jonathan F. Donges, and Jakob Runge. Using causal effect networks to analyze different arctic drivers of midlatitude winter circulation. *Journal of Climate*, 29(11):4069–4081, 2016. doi: 10.1175/JCLI-D-15-0654.1. URL https://doi.org/10.1175/JCLI-D-15-0654.1.

Marlene Kretschmer, Dim Coumou, Laurie Agel, Mathew Barlow, Eli Tziperman, and Judah Cohen. More-persistent weak stratospheric polar vortex states linked to cold extremes. *Bulletin of the American Meteorological Society*, 99(1):49–60, 2018. doi: 10.1175/BAMS-D-16-0259.1. URL https://doi.org/10.1175/BAMS-D-16-0259.1.

Sun Lantao, Perlwitz Judith, and Hoerling Martin. What caused the recent warm arctic, cold continents trend pattern in winter temperatures? *Geophysical Research Letters*, 43(10):5345–5352, 2016. doi: 10.1002/2016GL069024. URL https://agupubs.onlinelibrary.wiley.com/doi/abs/10.1002/2016GL069024.

Ogi Masayo and Wallace John M. Summer minimum arctic sea ice extent and the associated summer atmospheric circulation. *Geophysical Research Letters*, 34(12), 2007. doi: 10.1029/2007GL029897. URL https://agupubs.onlinelibrary.wiley.com/doi/abs/10.1029/2007GL029897.

Ogi Masayo and Wallace John M. The role of summer surface wind anomalies in the summer arctic sea ice extent in 2010 and 2011. *Geophysical Research Letters*, 39(9), 2012. doi: 10.1029/2012GL051330. URL https://agupubs.onlinelibrary.wiley.com/doi/abs/10.1029/2012GL051330.

Honda Meiji, Inoue Jun, and Yamane Shozo. Influence of low arctic seaice minima on anomalously cold eurasian winters. *Geophysical Research Letters*, 36(8), 2008. doi: 10.1029/2008GL037079. URL https://agupubs.onlinelibrary.wiley.com/doi/abs/10.1029/2008GL037079.

Steele Michael and Dickinson Suzanne. The phenology of arctic ocean surface warming. *Journal of Geophysical Research: Oceans*, 121(9):6847–6861, 2016. doi: 10.1002/2016JC012089. URL https://agupubs.onlinelibrary.wiley.com/doi/abs/10.1002/2016JC012089.

Tjernstrm Michael, Shupe Matthew D., Brooks Ian M., Persson P. Ola G., Prytherch John, Salisbury Dominic J., Sedlar Joseph, Achtert Peggy, Brooks Barbara J., Johnston Paul E., Sotiropoulou Georgia, and Wolfe Dan. Warmair advection, air mass transformation and fog causes rapid ice melt. *Geophysical Research Letters*, 42(13):5594–5602, 2015. doi: 10.1002/2015GL064373. URL https://agupubs.onlinelibrary.wiley.com/doi/abs/10.1002/2015GL064373.

Masato Mori, Masahiro Watanabe, Hideo Shiogama, Jun Inoue, and Masahide Kimoto. Robust arctic sea-ice influence on the frequent eurasian cold winters in past decades. *Nature Geoscience*, 7, Oct 2014. doi: 10.1038/ngeo2277. URL http://dx.doi.org/10.1038/ngeo2277.

James Overland, Jennifer A. Francis, Richard Hall, Edward Hanna, Seong-Joong Kim, and Timo Vihma. The melting arctic and midlatitude weather patterns: Are they connected? *Journal of Climate*, 28(20):7917–7932, 2015. doi: 10.1175/JCLI-D-14-00822.1. URL https://doi.org/10.1175/JCLI-D-14-00822.1.

James E. Overland. A difficult arctic science issue: Midlatitude weather linkages. *Polar Science*, 10(3):210 – 216, 2016. ISSN 1873-9652. doi: https://doi.org/10.1016/j.polar.2016.04.011. URL http://www.sciencedirect.com/science/article/pii/S187396521630024X. ISAR-4/ICARPIII, Science Symposium of ASSW2015.

James E. Overland, Kevin R. Wood, and Muyin Wang. Warm arcticcold continents: climate impacts of the newly open arctic sea. *Polar Research*, 30(1):15787, 2011. doi: 10.3402/polar.v30i0.15787. URL https://doi.org/10.3402/polar.v30i0.15787.

Rasmus A. Pedersen, Ivana Cvijanovic, Peter L. Langen, and Bo M. Vinther. The impact of regional arctic sea ice loss on atmospheric circulation and the nao.

Journal of Climate, 29(2):889–902, 2016. doi: 10.1175/JCLI-D-15-0315.1. URL https://doi.org/10.1175/JCLI-D-15-0315.1.

J A Screen. Influence of arctic sea ice on european summer precipitation. *Environmental Research Letters*, 8(4):044015, 2013. URL http://stacks.iop.org/1748-9326/8/i=4/a=044015.

Tido Semmler, Ray McGrath, and Shiyu Wang. The impact of arctic sea ice on the arctic energy budget and on the climate of the northern mid-latitudes. *Climate Dynamics*, 39(11):2675–2694, Dec 2012. ISSN 1432-0894. doi: 10.1007/s00382-012-1353-9. URL https://doi.org/10.1007/s00382-012-1353-9.

Svetlana A. Sorokina, Camille Li, Justin J. Wettstein, and Nils Gunnar Kvamst. Observed atmospheric coupling between barents sea ice and the warm-arctic cold-siberian anomaly pattern. *Journal of Climate*, 29(2):495–511, 2016. doi: 10.1175/JCLI-D-15-0046.1. URL https://doi.org/10.1175/JCLI-D-15-0046.1.

Kawasaki Takao and Hasumi Hiroyasu. The inflow of atlantic water at the fram strait and its interannual variability. *Journal of Geophysical Research: Oceans*, 121(1):502–519, 2015. doi: 10.1002/2015JC011375. URL https://agupubs.onlinelibrary.wiley.com/doi/abs/10.1002/2015JC011375.

Eiji Watanabe, Jonaotaro Onodera, Motoyo Itoh, Shigeto Nishino, and Takashi Kikuchi. Winter transport of subsurface warm water toward the arctic chukchi borderland. *Deep Sea Research Part I: Oceanographic Research Papers*, 128:115 – 130, 2017. ISSN 0967-0637. doi: https://doi.org/10.1016/j.dsr.2017.08.009. URL http://www.sciencedirect.com/science/article/pii/S0967063716304010.

Martin Wegmann, Yvan Orsolini, and Olga Zolina. Warm arcticcold siberia: comparing the recent and the early 20th-century arctic warmings. *Environmental Research Letters*, 13 (2):025009, 2018. URL http://stacks.iop.org/1748-9326/13/i=2/a=025009.

Yang Wenchang and Magnusdottir Gudrun. Springtime extreme moisture transport into the arctic and its impact on sea ice concentration. *Journal of Geophysical Research: Atmospheres*, 122(10):5316–5329, 2016. doi: 10.1002/2016JD026324. URL https://agupubs.onlinelibrary.wiley.com/doi/abs/10.1002/2016JD026324.

Rebecca A. Woodgate. Increases in the pacific inflow to the arctic from 1990 to 2015, and insights into seasonal trends and driving mechanisms from year-round bering strait mooring data. *Progress in Oceanography*, 160:124 – 154,

2018. ISSN 0079-6611. doi: https://doi.org/10.1016/j.pocean.2017.12.007. URL http://www.sciencedirect.com/science/article/pii/S0079661117302215.

Cian Woods and Rodrigo Caballero. The role of moist intrusions in winter arctic warming and sea ice decline. *Journal of Climate*, 29(12):4473–4485, 2016. doi: 10.1175/JCLI-D-15-0773.1. URL https://doi.org/10.1175/JCLI-D-15-0773.1.

Haijun Yang and Haijin Dai. Effect of wind forcing on the meridional heat transport in a coupled climate model: equilibrium response. *Climate Dynamics*, 45(5): 1451–1470, Sep 2015. ISSN 1432-0894. doi: 10.1007/s00382-014-2393-0. URL https://doi.org/10.1007/s00382-014-2393-0.

Haijun Yang, Qing Li, Kun Wang, Yu Sun, and Daoxun Sun. Decomposing the meridional heat transport in the climate system. *Climate Dynamics*, 44(9): 2751–2768, May 2015. ISSN 1432-0894. doi: 10.1007/s00382-014-2380-5. URL https://doi.org/10.1007/s00382-014-2380-5.

Huang Yiyi, Dong Xiquan, Xi Baike, Dolinar Erica K., and Stanfield Ryan E. The footprints of 16year trends of arctic springtime cloud and radiation properties on september sea ice retreat. *Journal of Geophysical Research: Atmospheres*, 122(4):2179–2193, 2016. doi: 10.1002/2016JD026020. URL https://agupubs.onlinelibrary.wiley.com/doi/abs/10.1002/2016JD026020.

Jing Zhang, Steve T Stegall, and Xiangdong Zhang. Windsea surface temperaturesea ice relationship in the chukchibeaufort seas during autumn. *Environmental Research Letters*, 13(3):034008, 2018. URL http://stacks.iop.org/1748-9326/13/i=3/a=034008.

Jinping Zhao, David Barber, Shugang Zhang, Qinghua Yang, Xiaoyu Wang, and Hongjie Xie. Record low sea-ice concentration in the central arctic during summer 2010. *Advances in Atmospheric Sciences*, 35(1):106–115, Jan 2018. ISSN 1861-9533. doi: 10.1007/s00376-017-7066-6. URL https://doi.org/10.1007/s00376-017-7066-6.

Linhao Zhong, Lijuan Hua, and Dehai Luo. Local and external moisture sources for the arctic warming over the barentskara seas. *Journal of Climate*, 31(5):1963–1982, 2018. doi: 10.1175/JCLI-D-17-0203.1. URL https://doi.org/10.1175/JCLI-D-17-0203.1.

M. rthun, T. Eldevik, L. H. Smedsrud, . Skagseth, and R. B. Ingvaldsen. Quantifying the influence of atlantic heat on barents sea ice variability and retreat. *Journal of Climate*, 25(13):4736–4743, 2012. doi: 10.1175/JCLI-D-11-00466.1. URL https://doi.org/10.1175/JCLI-D-11-00466.1.